

THESIS FOR THE DEGREE OF LICENTIATE OF ENGINEERING

Energy Efficiency of an Electric Vehicle Propulsion  
Inverter Using Various Semiconductor Technologies

ALI RABIEI



Division of Electric Power Engineering  
Department of Energy and Environment  
Chalmers University of Technology  
Göteborg, Sweden, 2013

# Energy Efficiency of an Electric Vehicle Propulsion Inverter Using Various Semiconductor Technologies

ALI RABIEI

Copyright ©2013 Ali Rabiei

Division of Electric Power Engineering  
Department of Energy and Environment  
Chalmers University of Technology  
Göteborg, Sweden

Printed by Chalmers Reproservice,  
Göteborg, Sweden 2013.

*To my family and friends*



# Abstract

In this Licentiate thesis, various solutions to improve the efficiency in the electrical vehicle drive drive line such as in the propulsion inverter and in the electric machine, are proposed and their benefits are quantified from an energy efficiency point of view. The efficiency analysis is based on modeling of a power electronics inverter, an electric machine and a battery in various drive cycles of an electric vehicle.

A solution to improve the efficiency in the electric machine is proposed. A loss minimizing optimized current vector control is suggested for a PMSM which minimizes the total machine losses. The solution has for the investigated electric machine up to 8% efficiency improvement or 1.5% improvement in average efficiency of various drive cycles such as ECE, EUDC and US06.

Several solutions are studied for the propulsion inverter. It is shown that by replacing the ordinary silicon pn freewheeling diodes in the propulsion inverter with SiC diodes, an average efficiency improvement of about 0.5 percent can be expected in various drive cycles. Furthermore by replacing the Silicon IGBTs in the inverter with SiC MOSFETs, the drive cycle efficiency in various drive cycles can be increased between 4 to 6 percents.

Finally a controllable dc-link voltage for the propulsion inverter is investigated in order to qualify the energy efficiency gain for the inverter and the motor. Their drive cycle energy efficiency improvement is 0.5 to 1 percent when using a SiC based inverter and 4 to 6 percents for an IGBT based inverter.

## Keywords

Energy efficiency, Loss calculation, Vehicle applications, Power electronics, Electric machines, Silicon carbide, Dc-link, Drive cycles, Nonlinear Optimization, Current vector control



# Acknowledgment

The financial support from the Swedish Energy Agency is gratefully appreciated.

I would like to take this opportunity to thank my supervisor and examiner Torbjörn Thiringer. His great emphasis on educating a researcher is very appreciated. I would also like to thank my supervisor Mikael Alatalo for his great technical contributions and useful discussions.

I would like to thank all my fellow colleagues in the division of Electric Power Engineering and all my Master's thesis students who have now left Chalmers. They have all created a fantastic working environment for me either by contributing with a single technical detail or by simply bringing up a smile on my face. Thank you all!

Finally I would like to thank my family whose support started before I could even remember and it has never stopped!

Ali Rabiei  
Göteborg, 2013





# List of Publications

- [I] Rabiei, A. ; Thiringer, T. ; Lindberg, J. , "Maximizing the energy efficiency of a PMSM for vehicular applications using an iron loss accounting optimization based on nonlinear programming,"  
*XXth International Conference on Electrical Machines, ICEM 2012, Marseille, France, 2-5 Sept. 2012*
  
- [II] Raee, H. ; Rabiei, A. ; Thiringer, T. , "Analytical prediction of switching losses in MOSFETs for variable drain-source voltage and current applications"  
*IEEE Conference on Industrial Electronics and Applications, ICIEA 2013, Melbourne, Australia, 19-21 June 2013*
  
- [III] Haghbin, S ; Rabiei, A. ; Grunditz, E. , "Switched Reluctance Motor in Electric or Hybrid Vehicle Applications: A Status Review"  
*IEEE Conference on Industrial Electronics and Applications, ICIEA 2013, Melbourne, Australia, 19-21 June 2013*
  
- [IV] Vindel, D. ; Haghbin, S. ; Rabiei, A. ; Carlson, O. ; Ghorbani, R. , "Field-Oriented Control of a PMSM Drive System Using the dSPACE Controller"  
*IEEE International Electric Vehicle Conference, IEVC 2012, Greenville, SC, 4-8 March 2012*



# Contents

<b>Abstract</b>	<b>v</b>
<b>Acknowledgment</b>	<b>vii</b>
<b>List of Publications</b>	<b>ix</b>
<b>1 Introduction</b>	<b>1</b>
1.1 Background and previous work . . . . .	1
1.2 Purpose of the thesis and contributions . . . . .	3
1.3 Thesis outline . . . . .	3
<b>2 Theory and Modeling of the Electric Drive System</b>	<b>5</b>
2.1 Permanent Magnet Synchronous Machine . . . . .	5
2.1.1 Steady state model of a PMSM . . . . .	5
2.1.2 Steady state PMSM model considering the core losses . .	6
2.2 Power electronics converters . . . . .	8
2.2.1 Conduction losses in switches . . . . .	8
2.2.2 Approximate modeling of the switching losses . . . . .	9
2.2.3 Switching process in MOSFET . . . . .	11
2.2.4 Turn-on process . . . . .	12
2.2.5 Turn-off process . . . . .	15
2.3 Electrical modeling of battery . . . . .	17
2.4 Static relation of the electric machine versus the vehicle movement	17
<b>3 Case Setup</b>	<b>19</b>
3.1 Electric Machine . . . . .	19
3.1.1 Scaled electric machine . . . . .	19
3.1.1.1 Electric machine for a system with 400 dc-link voltage . . . . .	20

3.1.1.2	Electric machine for a system with a variable dc-link voltage . . . . .	22
3.2	Inverter . . . . .	25
3.3	Switching losses in the used SiC MOSFET . . . . .	27
3.3.1	Measurement and simulation of turn on process . . . . .	27
3.4	Battery specification . . . . .	31
3.5	Vehicle specification . . . . .	31
3.6	Drive cycles . . . . .	32
<b>4</b>	<b>Energy Efficiency Improvement in Salient Permanent Magnet Synchronous Machines</b>	<b>35</b>
4.1	Zero d-current control strategy . . . . .	36
4.2	Maximum torque per ampere control strategy . . . . .	36
4.2.1	Extraction of ideal current vector of PMSM . . . . .	36
4.3	Loss minimization strategy . . . . .	38
4.3.1	Non-linear programming . . . . .	38
4.4	Comparison of different control strategies . . . . .	40
4.4.1	Comparison of different control strategies for an ideal machine without core loss . . . . .	40
4.4.2	Comparison of different control strategies for a machine with core loss . . . . .	41
4.4.3	Implementation of a variable $R_c$ in loss minimization optimization method . . . . .	43
4.4.4	Comparison of different drive cycles in simulation of an electric vehicle with nonlinear loss minimization strategy . . . . .	44
<b>5</b>	<b>System Level Efficiency Analysis of using different components and voltage levels</b>	<b>51</b>
5.1	Silicon Carbide Schottky freewheeling diode instead of a Silicon pn diode . . . . .	52
5.2	Change of the dc-link voltage level from 400V to 800V . . . . .	56
5.3	Silicon Carbide MOSFET as main switching device . . . . .	59
5.3.1	Effect of switching frequency on the component selection . . . . .	63
5.4	Overdimensioning of components in the inverter . . . . .	64
5.4.1	Overdimensioned Silicon IGBT . . . . .	64
5.4.2	Overdimensioned SiC MOSFET . . . . .	67
5.5	System level efficiency analysis in a propulsion inverter with a controllable dc-link voltage . . . . .	71
5.5.1	Ordinary system without a possibility to control the dc-link voltage . . . . .	74

---

5.5.2 Ordinary system with a controlled variable dc-link voltage system . . . . .	77
<b>6 Conclusions and Future Work</b>	<b>81</b>
6.1 Conclusions . . . . .	81
6.2 Future Work . . . . .	83
<b>Bibliography</b>	<b>85</b>



# Chapter 1

## Introduction

The first electric car was invented more than a century ago. However it was soon suppressed by conventional cars with combustion engines [1]. Nevertheless the recent environmental awareness, continuous oil price increase and national or European legislations such as the 20-20-20 target [2], have driven the research on new solutions to decrease the emissions and to improve the efficiency of the vehicles.

### 1.1 Background and previous work

Electric motors and power electronic devices such as dc to ac inverters are inherent parts of any electrified vehicles. Through the use of new materials, new topologies and new control strategies, it is possible to improve the efficiency of the electric machine and the power electronic components located in the electric vehicle. Since both the electric motor and power electronic devices have already relatively high efficiency, any efficiency improvement solution may not be extremely high. However, the electricity used by these components is stored in the battery and batteries in general are the most expensive electric components in the electric vehicles. This means that the electric energy available in the car is highly valuable and should be used with utmost care.

All electric vehicles should have at least one electric propulsion machine. Regarding its control strategies, an efficient control strategy for an electric machine should apart from having high performance dynamic, also minimize the losses in the machine. In permanent magnet synchronous machines, the Maximum Torque Per Ampere(MTPA) control method is a popular choice in many applications [3]. However, a question is how energy efficient this method performs when the core losses are also considered. There have been

different suggestions to compensate for its deficiency. In [4, 5] a model of a PMSM including the core loss is used to derive an analytical equation for the calculation of the current vectors. In [6, 7] the same model of a PMSM is used and a weighting factor is proposed to get the current vectors which produce even lower losses. However, a fully optimized model based current vector control and quantification of how much energy that could be gained by using an energy optimized control instead of a MTPA strategy for various drive cycles, is missing. In this thesis the use of a nonlinear programming optimization and an ordinary MTPA control are compared and the efficiency and losses in an electric vehicle for some selected driving cycles are quantified [8].

Design consideration of the power electronic components used in a propulsion inverter is an area with substantial research interest. In [9] for instance, different topologies, switching frequencies, voltage levels are investigated for a propulsion inverter in an electric vehicle. New semiconductor materials such as SiC, GaN have emerged and are suggested for vehicular applications [10, 11]. As a result, it is crucial to further investigate the possibility of new technologies and solutions to improve the efficiency and to lower the costs. Since SiC components have different characterization in comparison with Si devices such as higher band gap and thermal conductivity and the possibility for quicker switchings, it is important to characterize these devices. In [12] a SiC Shottky, in [13–15] SiC MOSFETs, JFETs and BJTs and in [16] a combinations of both Si and SiC devices are characterized. In [17], the total losses for two different JFET SiC based inverters are evaluated, however, the results are not put in a vehicular content. In [10] the impact of using SiC devices for propulsion inverters used in hybrid vehicles is investigated using a comprehensive vehicle model from the drive cycle to the battery, however, the switching losses are assumed to be solely dependant on the current. In this thesis a wider loss model is presented which includes the diode reverse recovery and switching dependency on the applied voltage. Moreover, the inverter operating points are established using an appropriate electric motor whose control strategy is also developed and optimized for the vehicle application.

With respect to new topology solutions, a DC/DC converter can be used between the battery and the inverter. Depending on the configuration, this converter adds an extra flexibility to the electric system. It will be possible to connect a low voltage battery to a high voltage drive system including an inverter and a motor. It will also make it possible to control the input dc-link of the inverter regardless of the battery voltage to ensure higher efficiency in the inverter, or higher performance of drive system. Several DC/DC converter topologies are designed and proposed in [18–21] In this thesis the en-



ergy efficiency consequence of using a controllable dc-link voltage, which can be achieved by a DC/DC converter, is studied for the propulsion inverter and the electric machine.

## 1.2 Purpose of the thesis and contributions

The main objective of the work reported in this thesis is to present methods in which the energy efficiency in an electric drive system of an electrified vehicle can be evaluated and to establish the energy efficiency of various technologies. The contributions in this work can be listed as

- Mathematical modeling of an electric machine and power electronic converters in an combined approach for system level loss analysis.
- Quantification of energy efficiency improvement in an electric drive system by deriving the current reference vectors using a optimized loss minimizing method which accounts for iron losses.
- Quantified energy efficiency comparison of various semiconductor technologies for a propulsion inverter of a vehicle.
- Establishing the energy efficiency and performance consequences of using a variable dc-link voltage in the propulsion inverter in the electric drive system.

## 1.3 Thesis outline

In this thesis the theoretical background of modeling different components in an arbitrary electric vehicle is explained in Chapter 2. In Chapter 3 all components that are used in this thesis are parameterized. In Chapter 4 an optimized control method is proposed for the chosen electric motor to improve the motor efficiency. Furthermore the improvement is quantified for various drive cycles for an electric vehicle and the loss model is also used for calculation of the total electric system losses including the propulsion inverter in Chapter 5. In Chapter 5 different semiconductor technologies and voltage levels for the inverter are compared with each other and its impact is studied for different drive cycles for the vehicle. Finally the possibility of using a variable voltage level for the dc side of the propulsion inverter is also investigated.



# Chapter 2

## Theory and Modeling of the Electric Drive System

In this chapter the components which are investigated later in the thesis are modeled.

### 2.1 Permanent Magnet Synchronous Machine

To find a small and economical electric machine to fulfill the driving requirements for different vehicle application is an ongoing research. As of today permanent magnet synchronous motors (PMSM) are widely used in electric and hybrid vehicles due to their high power and torque capacities. A PMSM is a rotating electric machine where the stator is a classic three phase stator like that of an induction motor and the rotor has permanent magnets. In this respect, the PMSM is equivalent to an induction motor, however the air gap magnetic field is produced by permanent magnets instead. PM synchronous motors offer a number of advantages in designing modern motion control systems. The use of a permanent magnet to generate substantial air gap magnetic flux without any excitation current makes it possible to design highly efficient PM motors [22].

#### 2.1.1 Steady state model of a PMSM

Using d-q component theory is a convenient way for performing various kinds of analyses in the PMSM. Since the loss analysis is not dependent on the dynamic behavior of the machine, it is sufficient to model the machine in steady state. In steady state the terminal voltages of a PMSM machine, can in dq-component

form analysis( $U_{sd}$  and  $U_{sq}$ ) be written as a function of terminal currents ( $I_{sd}$  and  $I_{sq}$ ) as

$$U_{sd} = R_s I_{sd} - \omega_{el} L_q I_{sq} \quad (2.1)$$

$$U_{sq} = R_s I_{sq} + \omega_{el} L_d I_{sd} + \omega_{el} \Psi_m \quad (2.2)$$

where

- $R_s$  stator resistance
- $\omega_{el}$  electrical angular speed
- $L_q$  equivalent q-axis inductance
- $L_d$  equivalent d-axis inductance
- $\Psi_m$  permanent magnet flux density

The torque is formed as

$$T_e = \frac{3}{2} p [\Psi_m I_{sq} + (L_d - L_q) I_{sq} I_{sd}] \quad (2.3)$$

### 2.1.2 Steady state PMSM model considering the core losses

Core losses in a PMSM machine generally consists of hysteresis losses, eddy current losses that can be formulated as [23]

$$P_{Fe} = k_{hyst} f B^2 + k_{eddy} f^2 B^2 + k_{ex} P_{ex} \quad (2.4)$$

where

- $f$  electrical frequency
- $B$  amplitude of the flux density
- $k_{hyst}$  hysteresis constant
- $k_{eddy}$  eddy current constant
- $k_{ex}$  excessive core loss constant
- $P_{ex}$  excessive core losses

It is convenient to model the core losses as a parallel resistor in the equivalent circuit. The core loss resistance( $R_c$ ) can simply be calculated by dividing the back EMF by the power loss for a given speed as

$$R_c = 3 \frac{(\omega_{el} \Psi_m)^2}{P_{Fe}} \quad (2.5)$$

The steady state equivalent circuits of the PMSM in the d-q system considering core losses are illustrated in Fig. 2.1.

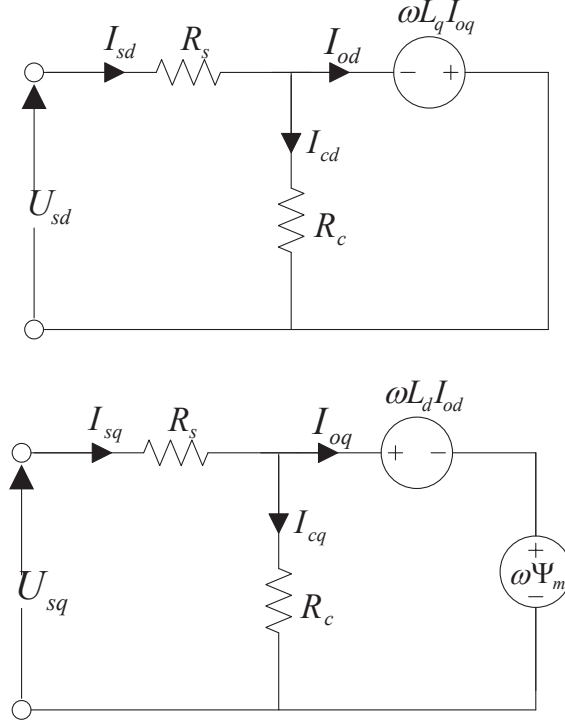


Figure 2.1: Equivalent d-q circuits of PMSM in the steady state considering core losses

The equations corresponding to the equivalent circuits are written as

$$U_{sd} = R_s I_{sd} - \omega_{el} L_q I_{oq} \quad (2.6)$$

$$U_{sq} = R_s I_{sq} + \omega_{el} L_d I_{od} + \omega \Psi_m \quad (2.7)$$

and

$$I_{od} = I_{sd} - I_{cd} = I_{sd} - \frac{\omega_{el} L_q I_{oq}}{R_c} \quad (2.8)$$

$$I_{oq} = I_{sq} - I_{cq} = I_{sq} - \frac{\omega_{el} L_d I_{od} + \omega_{el} \Psi_m}{R_c} \quad (2.9)$$

By using (2.8) and (2.9) as well as (2.6) and (2.7) and some simplification, the following expressions are found

$$U_{sd} = \left( R_s + \frac{\omega_{el}^2 L_d L_q}{R_c} \right) I_{sd} - \omega_{el} L_q I_{sq} + \frac{\omega_{el}^2 L_q \Psi_m}{R_c} \quad (2.10)$$

$$U_{sq} = \left(R_s + \frac{\omega_{el}^2 L_d L_q}{R_c}\right) I_{sq} + \omega_{el} L_d I_{sd} + \omega_{el} \Psi_m \quad (2.11)$$

The expression for the torque in this model is

$$T_e = \frac{3}{2} p (\Psi_m I_{oq} + (L_d - L_q) I_{od} I_{oq}) \quad (2.12)$$

## 2.2 Power electronics converters

Power electronics converters have the duty of transforming the electrical power from a certain voltage-current form into another one. The resulting losses in the converters are mainly due to conduction losses and switching losses in the semiconductors making up a converter. In a vehicle, a three phase propulsion inverter, converts the electric energy from the dc side (battery or DC/DC converter) to the ac side which is the electric motor. In Fig. 2.2 a conventional three phase inverter is shown.

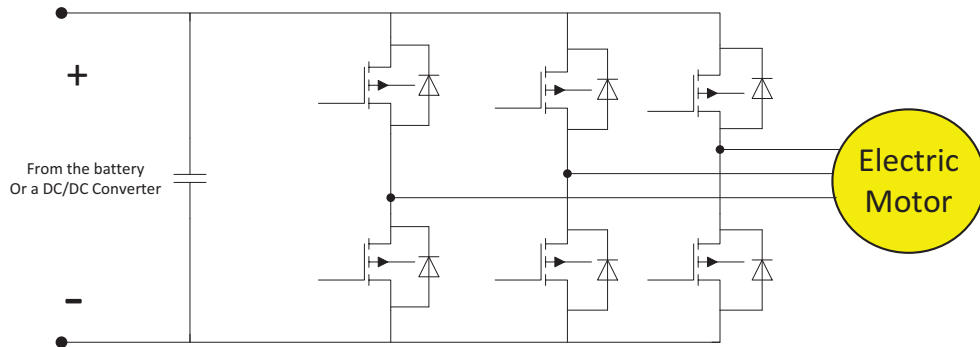


Figure 2.2: A conventional three phase inverter.

### 2.2.1 Conduction losses in switches

Conduction losses in semiconductors are the losses which occur during the static operation of the switches. The time length is long enough so that the components can be modeled by their forward characterization ( $v_{ds} = f(i_{ds})$ )

and the dynamics of the switches can be neglected. Furthermore the forward characteristic can be linearized and be modeled as a constant voltage drop ( $V_{ds,0}$ ) and a resistor ( $R_{on}$ ) and still obtain a good representation of the forward characterization in the switch as

$$v_{ds} = V_{ds,0}i_{ds} + R_{on}i_{ds}^2 \quad (2.13)$$

The inverter conduction loss will, however, depend on the power factor ( $\phi$ ) as well as the modulation index ( $m_a$ ) in the PWM modulator. The conduction loss for one switch and one diode shown in Fig. 2.2 is determined in [24] as

$$P_{Conduction,Switch} = \frac{V_{ds,0}I_m}{2\pi}(1 + \frac{\pi}{4}m_a \cos \phi) + \frac{R_{on}I_m^2}{2\pi}(\frac{\pi}{4} + \frac{2m_a}{3} \cos \phi) \quad (2.14)$$

where  $I_m$  is the peak value of the phase current. Similarly, the freewheeling diode can be modeled as

$$v_f = V_{f0}i_f + R_{on}i_f^2 \quad (2.15)$$

where  $V_{f0}$  is the constant voltage drop of the diode. Finally the conduction losses can be calculated as

$$P_{Conduction,Diode} = \frac{V_{ds,0}I_m}{2\pi}(1 - \frac{\pi}{4}m_a \cdot \cos \phi) + \frac{R_{on}I_m^2}{2\pi}(\frac{\pi}{4} - \frac{2m_a}{3} \cos \phi) \quad (2.16)$$

### 2.2.2 Approximate modeling of the switching losses

In order to make a loss analysis of power converters on a system level we need to have an approximate model for the switching waveforms which can provide switching losses in different operating conditions.

A first base approximation of switching losses is shown in Fig. 2.3 for a switch used in a half bridge with highly inductive load where currents and voltage rise and fall linearly between zero and their rated values.

While in turn off we might simply assume that the current and voltage change linearly from zero to their maximum value linearly, the turn on is affected by the current due to the reverse recovery of the freewheeling diode. As it can be seen in Fig. 2.3, the switching process during the turn-on can be divided into three parts.

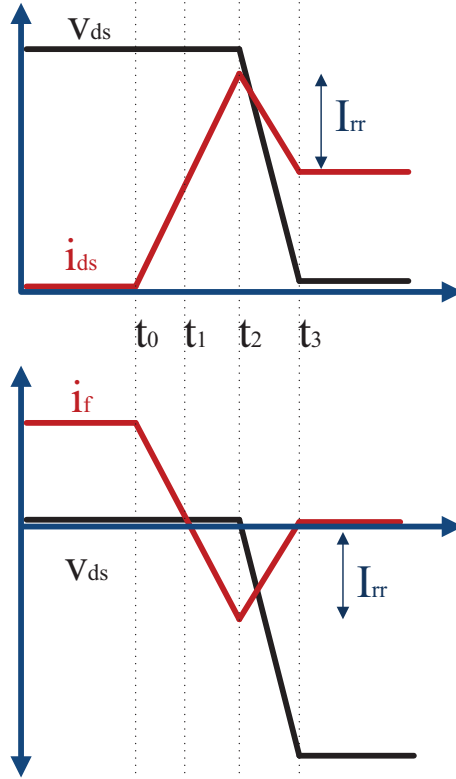


Figure 2.3: Approximate switching curves for a) the MOSFET b) the free-wheeling diode

The turn on switching loss energy can be calculated in three steps for the three time intervals shown in Fig. 2.3.

$$\begin{aligned}
 E_{on} &= \int_{t_0}^{t_1} v_{ds} i_{ds} = \int_{t_1}^{t_2} v_{ds} i_{ds} = \int_{t_2}^{t_3} v_{ds} i_{ds} \\
 &= \frac{V_{ds} I_{ds} (t_1 - t_0)}{2} \\
 &\quad + V_{ds} \left( I_{ds} + \frac{I_{rr}}{2} \right) (t_2 - t_1) \\
 &\quad + V_{ds} \left( \frac{I_{ds}}{2} + \frac{I_{rr}}{3} \right) (t_3 - t_2)
 \end{aligned} \tag{2.17}$$

Switching loss occurs when there is a non-zero voltage and current over the component. As a result the reverse recovery energy loss in the diodes only



occurs during the  $t_2$  to  $t_3$ . The integration over this time interval leads to

$$\begin{aligned} E_{rr} &= \int_{t_2}^{t_3} v_f i_f \\ &= \frac{V_f I_f t_{rr}}{6} \end{aligned} \quad (2.18)$$

The turn off loss is similarly calculated by

$$E_{off} = \frac{V_{ds} I_{ds} t_{off}}{2} \quad (2.19)$$

Finally the obtained switching energy loss, which are calculated for a specific  $V_{ds,ref}$  and  $I_{ds,ref}$ , can be predicted for other voltages  $v_{ds}$  and current  $i_{ds}$  using

$$E_{on} = E_{on,ref} \cdot \left(\frac{v_{ds}}{V_{ds,ref}}\right)^{k_{V,on}} \cdot \left(\frac{i_{ds}}{I_{ds,ref}}\right)^{k_{I,on}} \quad (2.20)$$

$$E_{rr} = E_{rr,ref} \cdot \left(\frac{v_{ds}}{V_{ds,ref}}\right)^{k_{V,rr}} \cdot \left(\frac{i_{ds}}{I_{ds,ref}}\right)^{k_{I,rr}} \quad (2.21)$$

$$E_{off} = E_{off,ref} \cdot \left(\frac{v_{ds}}{V_{ds,ref}}\right)^{k_{V,off}} \cdot \left(\frac{i_{ds}}{I_{ds,ref}}\right)^{k_{I,off}} \quad (2.22)$$

where  $k_{V,on}$ ,  $k_{V,off}$ ,  $k_{V,rr}$ ,  $k_{I,on}$ ,  $k_{I,off}$  and  $k_{I,rr}$  are coefficients that relate the losses calculated in the reference current and voltage to other currents and voltages. If such information exists in the datasheets, these coefficients can sometimes be derived from datasheets otherwise they are assumed to be one. This assumption leads to a linear dependence of switching losses on the current and voltage level.

### 2.2.3 Switching process in MOSFET

A good understanding of the switching losses requires a good understanding of the transients in semiconductor switching devices. IGBTs and MOSFETs are the most frequently used components in power electronic devices in an electrified vehicle. Besides, IGBTs and MOSFETs possess similar switching transient with one exception which is the tailing of the current in an IGBT during the turn off process. However the majority of IGBT datasheets include a sufficient switching loss data which are presented as a function of current and sometimes voltage. Hence this section focuses on MOSFET switching transients [25].

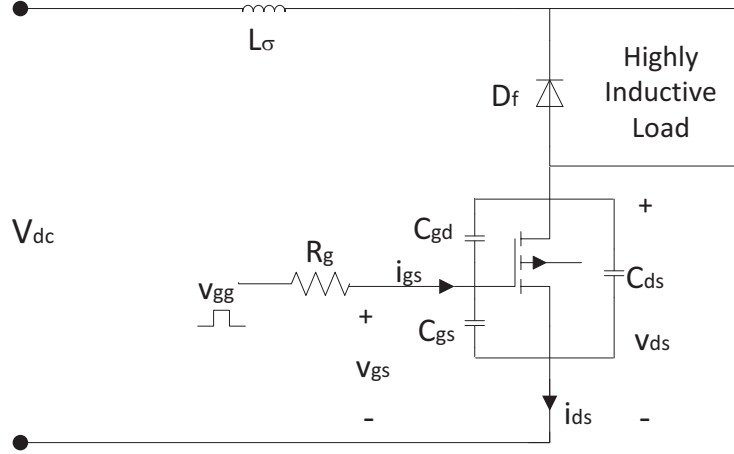


Figure 2.4: MOSFET transient modeling circuit

The transient model of a MOSFET which is described in [25] can be seen in Fig. 2.4. The model is a substantial simplification of more complex object. Furthermore  $L_\sigma$  which is the lumped parasitic inductance in the circuit is also included in the model.  $C_{ds}$ ,  $C_{gs}$  and  $C_{gd}$  are internal capacitances of the MOSFET. The values of these capacitances can vary depending on the applied voltage and can be expressed in terms of the datasheet parameters  $C_{iss}$ ,  $C_{oss}$ , and  $C_{rss}$  as

$$C_{gd} = C_{rss} \quad (2.23)$$

$$C_{gs} = C_{iss} - C_{rss} \quad (2.24)$$

$$C_{ds} = C_{oss} - C_{rss} \quad (2.25)$$

$$(2.26)$$

## 2.2.4 Turn-on process

The turn on process waveforms based on the model illustrated in Fig. 2.4 is shown in Fig. 2.5.

At the beginning, the device is off and the load current is passing through the free-wheeling diode. The initial conditions are:  $v_{gs} = 0$  V,  $v_{ds} = V_{dc}$  and  $i_{ds} = i_{gs} = 0$  A. At  $t = t_0$ ,  $V_{gg}$  is applied and the internal (and externally added) capacitors across the gate-source and gate-drain, starts to be charged through the gate resistor  $R_g$ . The gate-source voltage increases exponentially

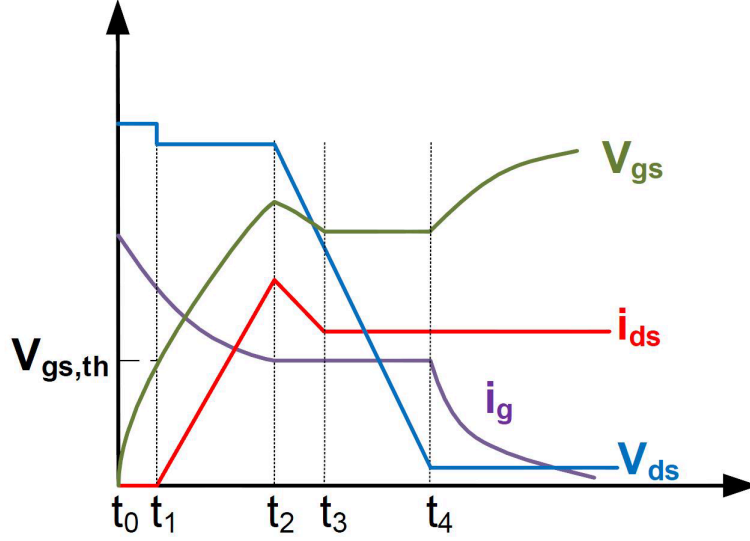


Figure 2.5: MOSFET turn-on waveforms

with the time constant  $\tau = R_g \cdot (C_{gs} + C_{gd})$ . The drain current remains zero until  $v_{gs}$  reaches the threshold voltage ( $V_{gs,th}$ ). The threshold voltage is the minimum gate-source voltage required before the drain-source current starts to increase during the turn on. The equations describing the current and voltage relations in the time interval  $t_0 - t_1$  are

$$\begin{aligned} i_{gs} &= \frac{V_{gg} - v_{gs}}{R_g} \\ &= C_{gs} \frac{dv_{gs}}{dt} - C_{gd} \frac{d(V_{gg} - v_{gs})}{dt} \\ \rightarrow \frac{V_{gg} - v_{gs}}{R_g} &= C_{gs} \frac{dv_{gs}}{dt} - C_{gd} \frac{d(V_{gg} - v_{gs})}{dt} \end{aligned} \quad (2.27)$$

$$\rightarrow v_{gs} = V_{gg}(1 - e^{-(t-t_0)/\tau}) \quad (2.28)$$

The delay time, which is the time that it takes for the gate-source voltage to reach the threshold voltage ( $v_{gs}(t_2) = V_{gs,th}$ ), is

$$t_d = -\tau \ln\left(1 - \frac{V_{gs,th}}{V_{gg}}\right) \quad (2.29)$$

When  $v_{gs}$  reaches the threshold voltage, the drain current starts to increase linearly causing the MOSFET's voltage to drop. At the same time the diode

becomes reverse biased and turns off. The equations during the time period  $t_1$ - $t_2$  are

$$v_{ds} = V_{dc} - (L_\sigma + L_d) \frac{di_{ds}}{dt} \quad (2.30)$$

$$i_{ds} = g_m(v_{gs} - V_{th}) \quad (2.31)$$

where  $g_m$  is the MOSFET forward transconductance and is a nonlinear factor which can be extracted from the datasheet of the switch.  $i_{ds}$  increases until it reaches the load current  $I_o$  or in case of having diode reverse recovery, until it reaches  $I_o + I_{rr}$ . The rise time of the drain current can be calculated as [26],

$$t_2 - t_1 = t_{on} = \tau \ln\left(\frac{g_m(V_{gg} - V_{gs,th})}{g_m(V_{gg} - V_{gs,th}) - (I_o + I_{rr})}\right) \quad (2.32)$$

During the time interval  $t_2$  to  $t_3$ , the reverse recovery takes place while  $v_{gs}$  decreases from  $v_{ds} = V_{gs,th} + \frac{I_o + I_{rr}}{g_m}$  to  $v_{ds} = V_{gs,th} + \frac{I_o}{g_m}$

At  $t_3$ , the MOSFET reaches the plateau level, the gate voltage and current become constant, all the gate current passes through the gate-drain capacitor, therefore the gate current will be

$$i_{gs} = -C_{gd} \frac{dv_{ds}}{dt} \quad (2.33)$$

Thus the drain-source voltage is

$$v_{ds} = -\frac{V_{gg} - V_{gs,th}}{R_g C_{gd}}(t - t_2) + V_{dc} \quad (2.34)$$

As soon as the drain-source voltage reaches the input voltage,  $v_{gs}$  increases to  $V_{gg}$  while  $i_g$  decreases until it reaches zero.

Finally at  $t_4$ , the MOSFET enters the steady state mode and operate according to its forward characteristic.

$$v_{ds} = R_{ds} I_o \quad (2.35)$$

where  $R_{ds}$  is the resistive behavior of the MOSFET according to its forward characteristic.

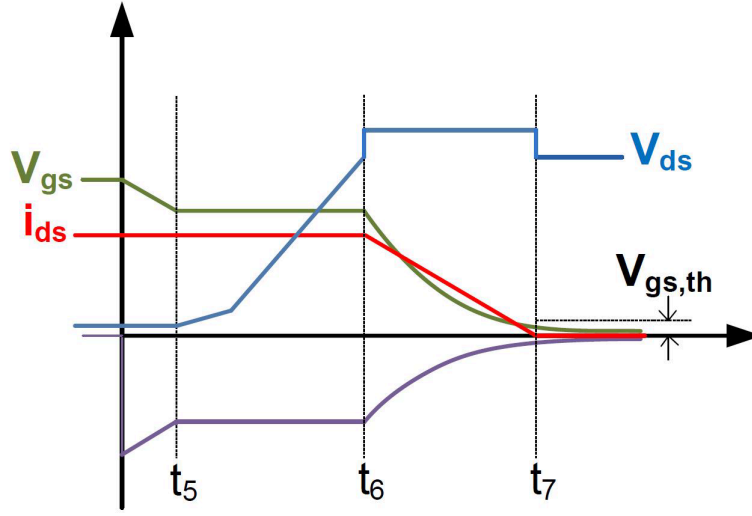


Figure 2.6: MOSFET turn-off waveforms

### 2.2.5 Turn-off process

The turn-off waveforms are shown in Fig. 2.6. The initial conditions for the turn-off period are  $v_{ds} = R_{ds}I_o$ ,  $v_{gs} = V_{gg}$ ,  $i_{gs} = 0$  and  $i_{ds} = I_o$ .

The turn-off process starts when the applied gate voltage falls, making the gate-source and gate-drain capacitors to discharge through  $R_g$ .  $i_{gs}$  can be obtained by

$$\begin{aligned} i_{gs} &= -\frac{V_{gg}}{R_g} \\ &= (C_{gs} + C_{gd}) \frac{dv_{gs}}{dt} \end{aligned} \quad (2.36)$$

Hence  $v_{gs}$  will be

$$v_{gs} = V_{gg} e^{-(t-t_0)/\tau} \quad (2.37)$$

$v_{gs}$  continues to decrease until it reaches the plateau level at  $t = t_5$ , while the drain current remains at the same level as the load current. The gate-source voltage at  $i_{ds} = I_o$  is

$$v_{gs} = \frac{I_o}{g_m} + V_{gs,th} \quad (2.38)$$

From (2.37) and (2.38) the time that it takes for  $v_{gs}$  to reach a constant

value can be obtained by

$$v_{gs} = \tau \frac{V_{gg}}{\frac{I_o}{g_m} + V_{gs,th}} \quad (2.39)$$

In the time interval  $t_5$ - $t_6$  since, the gate-source voltage is constant and all the current is taken from the gate-drain capacitor according to

$$\begin{aligned} i_{gs} &= C_{gd} \frac{dv_{gd}}{dt} \\ &= C_{gd} \frac{d(v_{gs} - v_{ds})}{dt} \\ &= -C_{gd} \frac{dv_{ds}}{dt} \end{aligned} \quad (2.40)$$

The gate current can be found as

$$i_g = \frac{V_{gs,th}}{R_g} = \frac{1}{R_g} \left( \frac{I_o}{g_m} + V_{gs,th} \right) \quad (2.41)$$

The drain-source voltage will be achieved by combining (2.40) and (2.41)

$$v_{ds} = R_{ds} I_o + \frac{1}{R_g C_{gd}} \left( \frac{I_o}{g_m} + V_{gs,th} \right) (t - t_1) \quad (2.42)$$

At the time  $t_6$  the drain-source voltage reaches the dc voltage, forcing the free-wheeling diode to be turned on. Hence the drain-source current  $i_{ds}$  starts falling and it is described according to

$$i_{ds} = g_m (v_{gs} - V_{gs,th}) \quad (2.43)$$

where  $v_{gs}$  is obtained from the following equation,

$$v_{gs} = \left( \frac{I_o}{g_m} + V_{gs,th} \right) e^{-(t-t_2)/\tau} \quad (2.44)$$

The current fall time is calculated by having the time constant and the threshold voltage over  $V_{gs}$  at load current

$$t_{fi} = -R_g C_{iss} \ln \frac{V_{gs,th}}{V_{gs,Io}} \quad (2.45)$$

While the current is falling, the parasitic inductance in the circuit ( $L_\sigma$ ) cause an overshoot in  $v_{ds}$  as

$$v_{ds} = V_{dc} + (L_\sigma + L_d) \frac{di_{ds}}{dt} \quad (2.46)$$

where the rate of changes of the current ( $\frac{di_{ds}}{dt}$ ) in the device is achieved by dividing the MOSFET load current over the current fall time.

$$\frac{di_{ds}}{dt} = \frac{I_o}{t_{fi}} \quad (2.47)$$

However it should be noted that the  $t_{fi}$  may not be necessarily decided by the MOSFET itself if the parasitic inductances in the drain-source loop are big enough to force a slower rate of current on both turn-on and turn-on.

Finally during the time interval  $t_6$ - $t_7$  the gate-source voltage reaches the threshold voltage ( $v_{gs}(t_7) = V_{gs,th}$ ). The gate-source voltage goes to zero and the MOSFET is fully turned off.

## 2.3 Electrical modeling of battery

Dynamic battery models are highly complex. The voltage source is a function of temperature and SOC, whereas the resistor is only a function of temperature. In this thesis the electric model consists of a voltage source and a resistance whereas the voltage source Open Circuit Voltage(OCV) is dependent on the State Of Charge(SOC), giving

$$V_t = OCV + R_{in} \cdot I \quad (2.48)$$

$$\frac{dSOC}{dt} = k \cdot I(t) \quad (2.49)$$

where

$$k = \frac{1}{Q_{rated} \cdot 3600} \quad (2.50)$$

## 2.4 Static relation of the electric machine versus the vehicle movement

In a vehicle model, torque and speed references from the drive cycle are transformed to torque and speed references for the electric machine through

$$F = ma + \frac{1}{2}\rho C_d A_f V_{ref}^2 + C_r mg + mg \sin \alpha \quad (2.51)$$

$$T_{motor} = \frac{F \cdot r_{wheel}}{R_{GB}} \quad (2.52)$$

$$V_{motor} = V_{ref} R_{GB} \frac{60}{3.6 \cdot 2 \cdot \pi \cdot r_{wheel}} \quad (2.53)$$

where  $F$  is the traction force,  $m$  is the vehicle mass,  $a$  is the vehicle acceleration,  $\rho$  is air density,  $C_d$  is air drag coefficient,  $A_f$  is the vehicle frontal area,  $V_{ref}$  is drive cycle speed reference in km/h,  $C_r$  is rolling resistance coefficient,  $\alpha$  is the road angle slope,  $T_{motor}$  is the torque on the machine,  $R_{GB}$  is the gearbox ratio and  $V_{motor}$  is the machine speed in revolutions per minute.



# Chapter 3

## Case Setup

In this chapter all the components that are used in other chapters are introduced.

### 3.1 Electric Machine

The electric machine used in this thesis is based on the machine developed in [27] with the parameters found in Table 3.1.

Table 3.1: Machine Parameters

Parameter	Value from [27]
$R_s$	0.0079 $\Omega$
$L_{sd}$	0.23 mH
$L_{sq}$	0.50 mH
$\Psi_m$	0.104
p	2 pole-pairs
$I_{max}$	360 A
$I_{maxcontinuous}$	180 A
$U_{max}$	320/ $\sqrt{3}$ V
$R_c$	variable $\Omega$

#### 3.1.1 Scaled electric machine

The electric motor specified in Section 3.1 is used for the analysis. However the original machine is built for a dc-link voltage of 320 V and in this thesis, electric

machines for a dc-link of 400V and 800V are required. This leads to scaling factors of 1.25 and 2.5 for the 400V and 800V dc-link systems respectively.

The scaling method ensures that the output characteristics of the motor like the maximum torque, speed and losses remain constant. This can be achieved by changing the motor parameters as specified in Table 3.2.

Table 3.2: Scaled machine parameters

Parameter	Scaled value
$R_s$	$0.0079 \cdot \text{ScalingFactor} \cdot \text{ScalingFactor} \Omega$
$L_{sd}$	$0.23 \cdot \text{ScalingFactor} \cdot \text{ScalingFactor} \text{ mH}$
$L_{sq}$	$0.50 \cdot \text{ScalingFactor} \cdot \text{ScalingFactor} \text{ mH}$
$\Psi_m$	$0.104 \cdot \text{ScalingFactor}$
p	2 pole-pairs
$R_c$	Variable
$I_{max}$	$360 / \text{ScalingFactor} \text{ A}$
$I_{maxcontinuous}$	$180 / \text{ScalingFactor} \text{ A}$
$U_{max}$ (Phase voltage)	$320 \cdot \text{ScalingFactor} / \sqrt{3} \text{ V}$

### 3.1.1.1 Electric machine for a system with 400 dc-link voltage

The resulting current and voltage levels as functions of torque and speed for the 1.25 scaled machine which is suitable for a 400 V dc-link voltage and the 2.5 scaled machine which is suitable for an 800 V dc-link voltage are shown in Fig. 3.1 and 3.2 respectively.

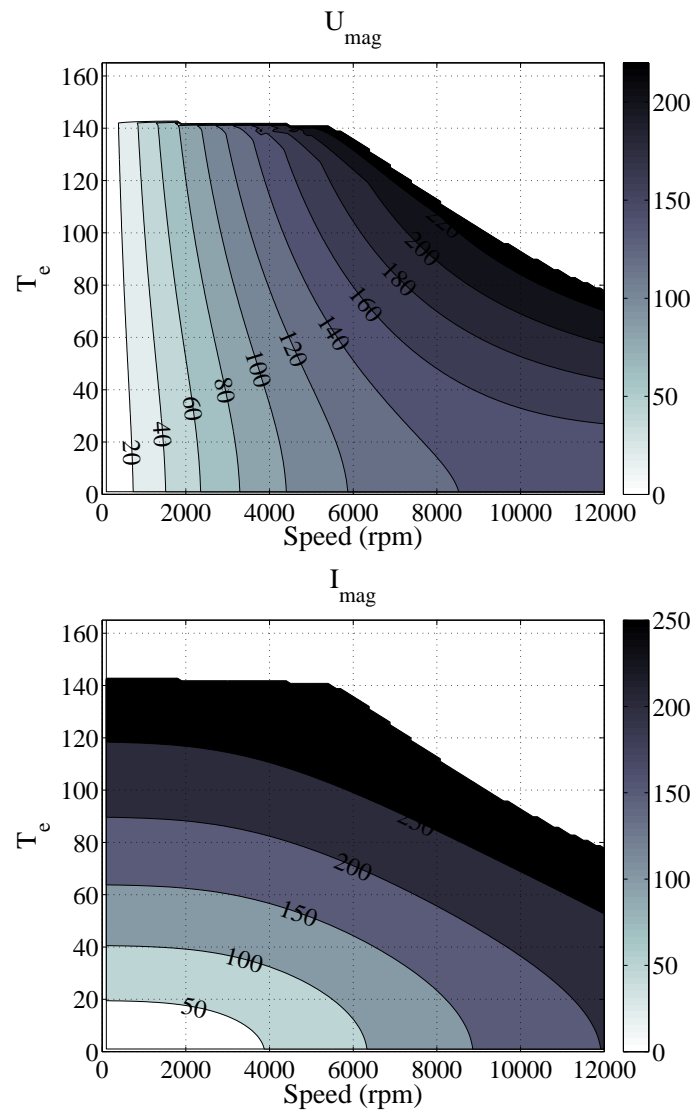


Figure 3.1: Magnitudes of the electric motor required phase current and voltage for a 400V dc-link voltage.

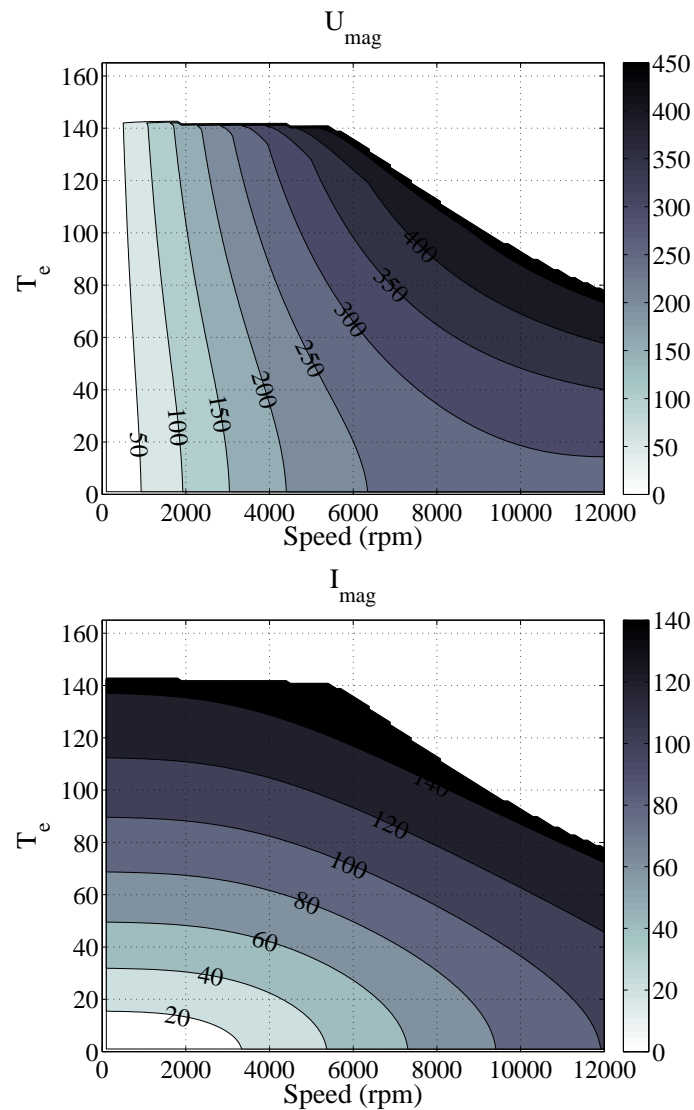


Figure 3.2: Magnitudes of the electric motor required phase current and voltage in a 800V dc-link voltage.

### 3.1.1.2 Electric machine for a system with a variable dc-link voltage

The electric motor specified in Section 3.1 which is scaled for an 800 V dc-link voltage in Section 3.1.1 is in this section calculated for a variable dc-link voltage. The resulting current and voltage levels as functions of torque, speed and dc-link voltage is shown in Fig. 3.3 and 3.4 respectively.

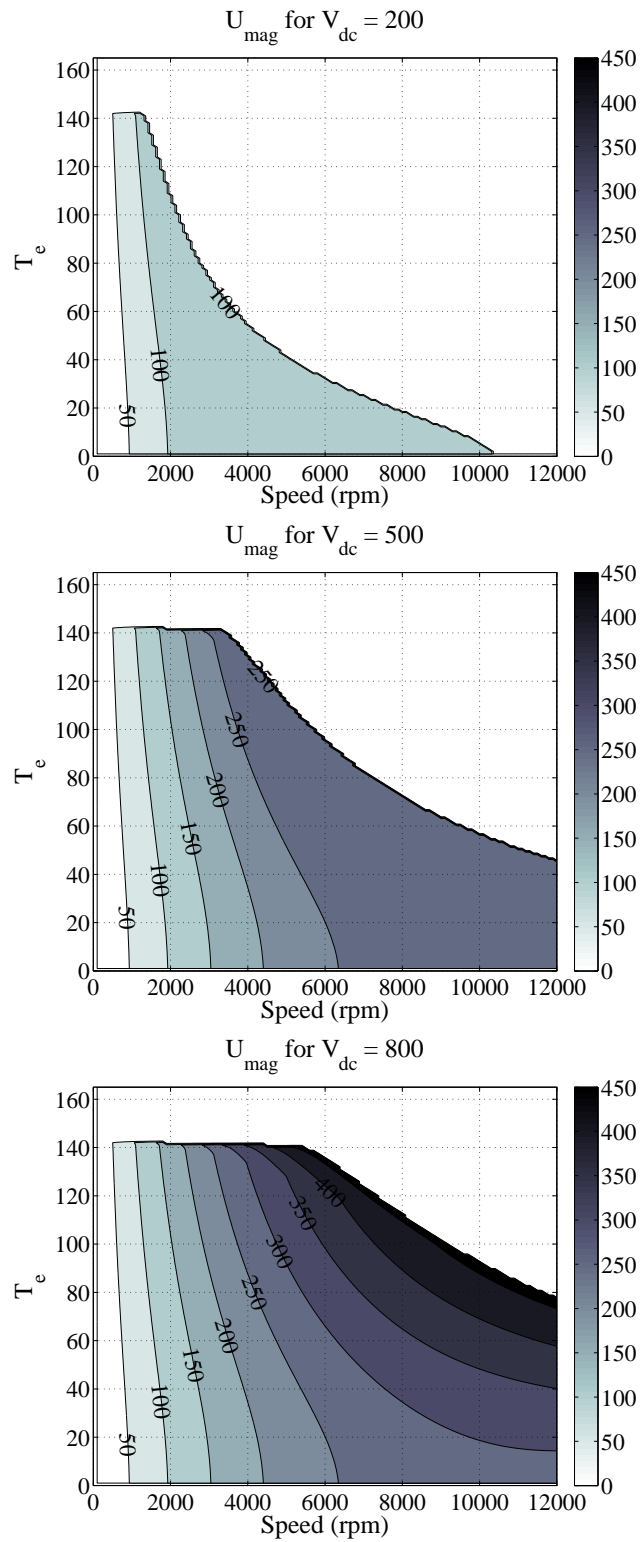


Figure 3.3: Magnitude of the electric motor required phase voltage for different dc-link voltages

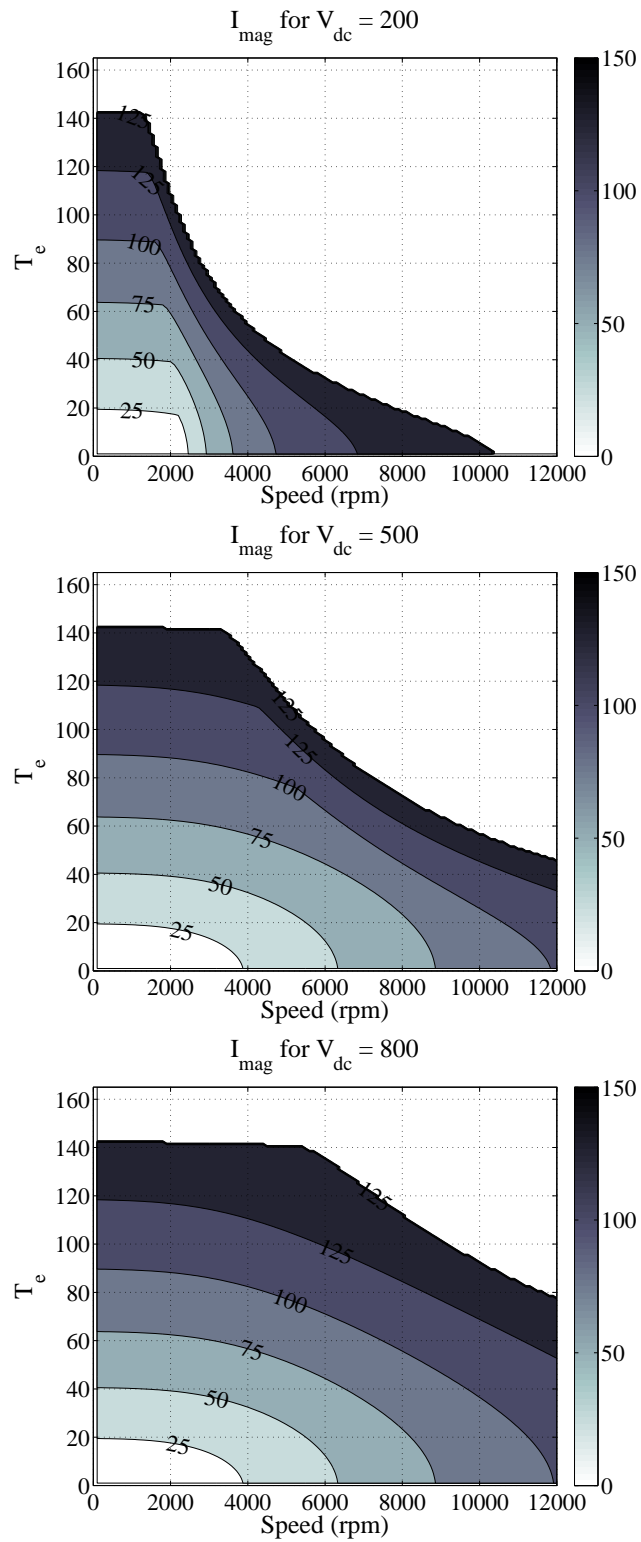


Figure 3.4: Magnitude of the electric motor required phase current for different dc-link voltages

## 3.2 Inverter

The dc-link voltage level of the electric system on the battery side is chosen to be 400 V or 800 V for power electronic components with breakdown voltage of 600 V and 1200 V respectively. This 200 V/400 V safety margin is chosen to give room for switching overvoltages due to parasitic inductances in the commutating circuit.

The components which are used in the converter for different analysis are listed below.

- 600V silicon IGBT with pn diode (FS600R07A2E3)
- 600V silicon IGBT with SiC schottky diode (FS600R07A2E3 with SCS220AG)
- 1200V silicon IGBT with pn diode (CM3000EXS-24S)
- 1200V SiC MOSFET with SiC diode (SCH2080KE)

The parameters required for loss calculation for each component is gathered in Table 3.3.

In order to obtain an identical power rating for all components, some components are put in parallel to reach the desired power rating. However those components in parallel are assumed to be one module. So the technical issues regarding the use the parallel components are ignored. The name of these new modules consists of the name of the module they are made of, followed by a number and 'X'. This means for example that, MOSFET (SCH2080KE)10X, is one module which consists 10 MOSFET (SCH2080KE) in parallel. Consequently the forward and switching characteristics values mentioned in Table 3.3, are for the resulting module.

$E_{off}$  and  $E_{on}$  shown in Table 3.3 for MOSFET (SCH2080KE)10X, are calculated in (3.6).

Table 3.3: Components characteristics based on datasheet and calculation  
@ $T_j = 120C - 150C$  [28–32]

Components	Breakdown Voltage	Forward Characteristics	Switching Characteristics
Si IGBT (FS600R07A2E3)	600V	$V_{ce,0} = 0.7V$ $R_{on} = 1.75 m\Omega$	$E_{on} = 11.5mJ, E_{off} = 18.5mJ$ @ $V_{ce} = 300V, @I_{ce} = 400A$
Si pn diode for (FS600R07A2E3)	600V	$V_{f,0} = 0.9V$ $R_{on} = 0.9 m\Omega$	$E_{rr} = 8.5mJ$ @ $V_R = 300V, @I_f = 400A$
SiC schottky diode (SCS220AG)30X	650V	$V_{f,0} = 0.9V$ $R_{on} = 2.6 m\Omega$	$E_{rr} = 0.093mJ$ @ $V_R = 400V, @I_f = 300A$
Si IGBT (CM3000EXS-24S)	1200V	$V_{ce,0} = 0.8V$ $R_{on} = 2 m\Omega$	$E_{on} = 41mJ, E_{off} = 32mJ$ @ $V_{ce} = 600V, @I_{ce} = 300A$
Si pn diode for (CM3000EXS-24S)	1200V	$V_{f,0} = 0.6V$ $R_{on} = 4.5 m\Omega$	$E_{rr} = 22mJ$ @ $V_R = 600V, @I_f = 300A$
SiC MOSFET (SCH2080KE)10X	1200V	$V_{ds,0} = 0V$ $R_{on} = 14.3 m\Omega$	$E_{on} = 3.1mJ, E_{off} = 0.56mJ$ @ $V_{ds} = 400V, @I_{ds} = 300A$
SiC diode for (SCH2080KE)10X	1200V	$V_{f,0} = 0.8V$ $R_{on} = 6 m\Omega$	$E_{rr} = 0.03mJ$ @ $V_R = 400V, @I_f = 300A$



### 3.3 Switching losses in the used SiC MOSFET

The circuit shown in Fig. 3.5 is used for measuring the switching waveforms.

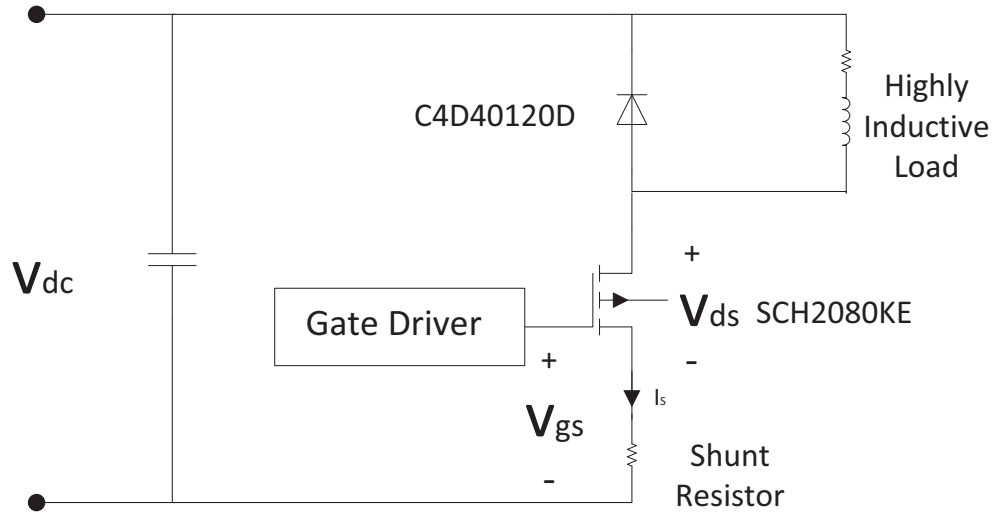


Figure 3.5: Measurement circuit

A SiC MOSFET(SCH2080KE) has been used in an evaluation circuit for measurement of the switching process. The freewheeling diode is a SiC Schotky diode(C4D40120D).

Instead of using a Rogowski coil for measuring the drain current a shunt resistor is chosen. Since the dc value of the current  $i_{ds}$  as well as the accurate delay time between  $v_{ds}$  and  $i_{ds}$  are very important for loss calculations, the use of a shunt resistance is preferred over a Rogowski coil. The voltage over the resistor is interpreted as current, as long as the measured  $R_{shunt} \cdot i_{ds}$  is much higher than  $L_r \cdot \frac{di_{ds}}{dt}$ . The shunt resistor used in this measurement is measured around  $R_{shunt} = 1 \Omega$ ,  $L_{shunt} = 5 nH$ . Thus with a measurement of  $i_{ds} = 3 A$  and  $\frac{di_{ds}}{dt} = 30 A/\mu s$ , it is assured that the shunt resistor is behaving sufficiently resistive.

#### 3.3.1 Measurement and simulation of turn on process

The simulation is based on the equations explained in Section 2.2.3 with the dynamic parameters of the MOSFET and the diode extracted from their datasheets and initial conditions of  $V_{gg} = 12 V$  and  $R_g = 10\Omega$ .

Table 3.4: Switching loss comparison

Case	Datasheet parameters [32,33]
MOSFET (SCH2080KE)	$C_{rss,lv} = 50 \text{ pF}$ , $C_{rss,hv} = 100 \text{ pF}$ $C_{iss,lv} = 4500 \text{ pF}$ , $C_{iss,hv} = 1850 \text{ pF}$ $V_{gs,th} = 3 \text{ V}$ , $g_m = 0.8$ , $R_{g,in} = 6.5 \Omega$
Diode (C4D40120D)	$Q_{rr} = 130 \text{ nC}$

The datasheet parameters are converted to the parameters used in the theoretical equations needed in the simulation. However the capacitances of a MOSFET have a non-linear relation with the voltage. To avoid the effect on non-linearity in the simulation, two constant values for each capacitors are chosen. One constant value is used for high voltages, one constant value is used for low voltages. The border between the high and low voltage is  $10 \text{ V}$ .

$$C_{gd,lv} = C_{rss,lv} = 50 \text{ pF} \quad (3.1)$$

$$C_{gd,hv} = C_{rss,hv} = 100 \text{ pF} \quad (3.2)$$

$$C_{gs,lv} = C_{iss,lv} - C_{rss,lv} = 4450 \text{ pF} \quad (3.3)$$

$$C_{gs,hv} = C_{iss,hv} - C_{rss,hv} = 1750 \text{ pF} \quad (3.4)$$

$I_{rr}$  depends on the  $Q_{rr}$  of the freewheeling diode and  $\frac{di_{ds}}{dt} = \frac{t_{on}}{I_o}$ . It can be assumed that  $\frac{di_{ds}}{dt}$  remains constant until  $Q_{rr}$  in the diode is discharged. So by knowing the area of a triangle  $Q_{rr}$  and the relation between its two sides  $\frac{di_{ds}}{dt}$ , the height  $I_{rr}$  can be calculated as

$$I_{rr} \approx 3 \text{ A} \quad (3.5)$$

The simulated turn-on waveforms are calculated using (2.28) to (2.35). In Fig. 3.6 the turn on switching process and losses are illustrated for both the measurement and the simulation based on the theory explained in Section 2.2.3 with values extracted from the datasheet. It can be seen that the simulation can predict the actual waveform and losses relatively good during the turn-on.

In Fig. 3.7 the turn-off switching process is illustrated for both the measurement and the simulation. As it can be seen in Fig 3.7, the current falls earlier than predicted in the simulation. This could be due to the fact that

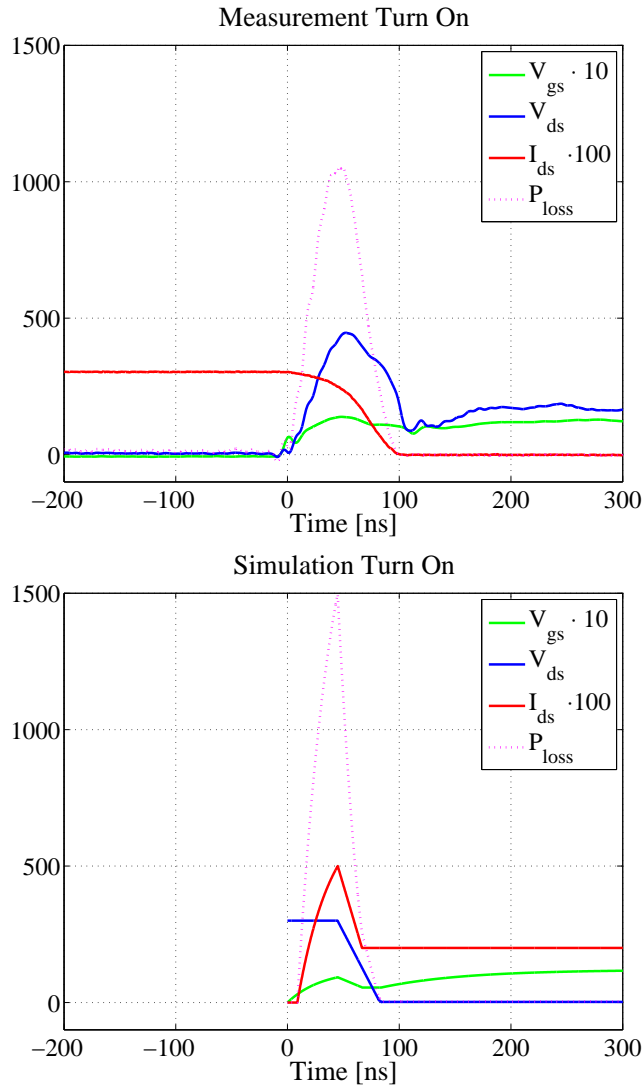


Figure 3.6: Measured and simulated turn on switching process

the simulation process does not take into account the effect of the capacitance of the diode and that the MOSFET output capacitors which behave like capacitive snubbers in ZVS (Zero Voltage Switching) circuits.

Finally the switching losses obtained from the measurement, detailed modeling and approximate modeling based on datasheet values are compared with each other and the results are shown in Table 3.5. The approximate switching losses for the reference values ( $V_{ds,ref} = 400V$  and  $I_{ds} = 10A$ ) are evaluated for the SiC MOSFET (SCH2080KE) based on (2.17) to (2.19) and the scaled

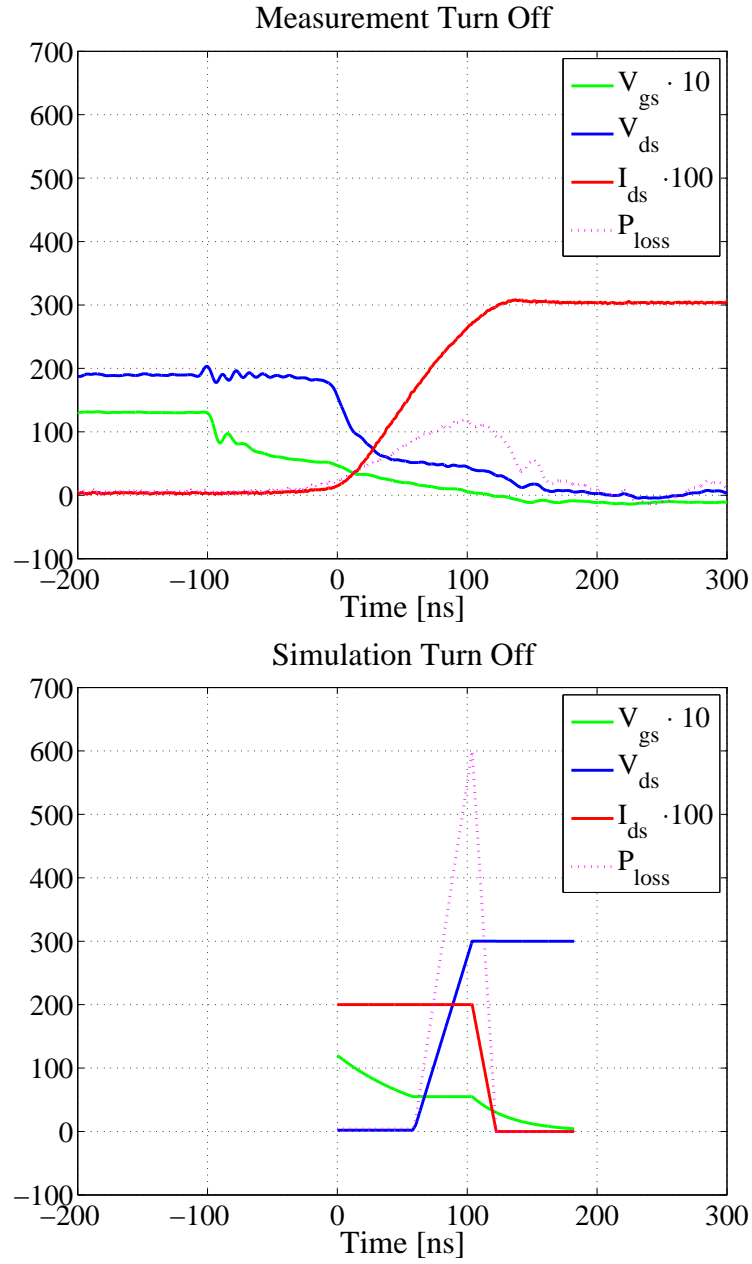


Figure 3.7: Measured and simulated turn off switching process

switching losses are calculated based on (2.20) to (2.22).

$$\begin{aligned}
 E_{on,ref} &= 311 \mu J \\
 E_{off,ref} &= 56 \mu J \\
 E_{rr,ref} &= 3 \mu J
 \end{aligned}
 \tag{3.6}$$

Table 3.5: Switching loss comparison

Case	Measurement	Simulation	Approximated method
Turn on for $V_{ds} = 300, I_{ds} = 2$	$52 \mu J$	$53 \mu J$	$47 \mu J$
Turn on for $V_{ds} = 150, I_{ds} = 2.5$	$25 \mu J$	$23 \mu J$	$29 \mu J$
Turn off for $V_{ds} = 300, I_{ds} = 2$	$10 \mu J$	$19 \mu J$	$8.5 \mu J$
Turn off for $V_{ds} = 150, I_{ds} = 2.5$	$4 \mu J$	$8.5 \mu J$	$5 \mu J$

The simulation and approximate method give a good approximation of switching losses during the turn-on while the turn-off loss is overestimated.

### 3.4 Battery specification

A battery with the specifications given in Table 3.7 is used in this thesis.

Table 3.6: Battery Specification

Parameter	Value
Internal resistance( $R_{in}$ )	$0.2 \Omega$
Rated charge capacity( $Q_{rated}$ )	$12.5 A \cdot h$
Initial voltage( $m$ )	$800 V$
Initial SOC( $SOC_{ini}$ )	$90 \%$

### 3.5 Vehicle specification

The vehicle used as a reference for simulations throughout the report is a typical midsize sedan vehicle specified in Table 3.7.

Table 3.7: Vehicle Parameters

Parameter	Value
Air density ( $\rho$ )	1.225 kg/m <sup>3</sup>
Air drag coefficient( $C_d$ )·Frontal area( $A_f$ )	0.6758 m <sup>2</sup>
Rolling resistance coefficient( $C_r$ )	0.009
Wheel radius( $W_r$ )	0.3 m
Vehicle mass( $m$ )	1700 kg
Gear box ratio( $R_{GB}$ )	10

### 3.6 Drive cycles

The drive cycles used in this thesis are shown in this section. ECE drive cycle shown in Fig. 3.10 is a relatively slow and low power demanding drive cycle while EUDC shown in Fig. 3.9 is more demanding and reaches the tops speed of 120 km/h. These two drive cycles, together form a drive cycle called NEDC which is a standard European drive cycle used in various legislations. US06 drive cycle shown Fig. 3.8 takes as much time as ECE and EUDC combined but has more realistic driving pattern with both urban and city driving combined.

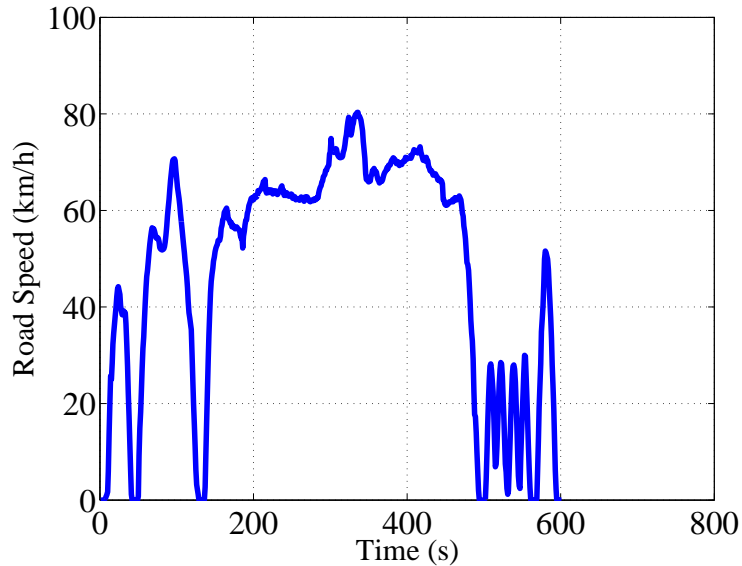


Figure 3.8: Drive cycle US06

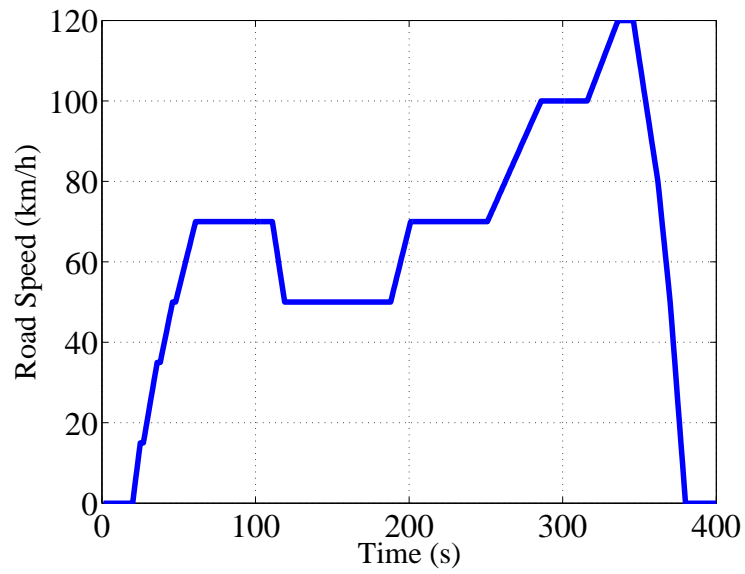


Figure 3.9: Drive cycle EUDC

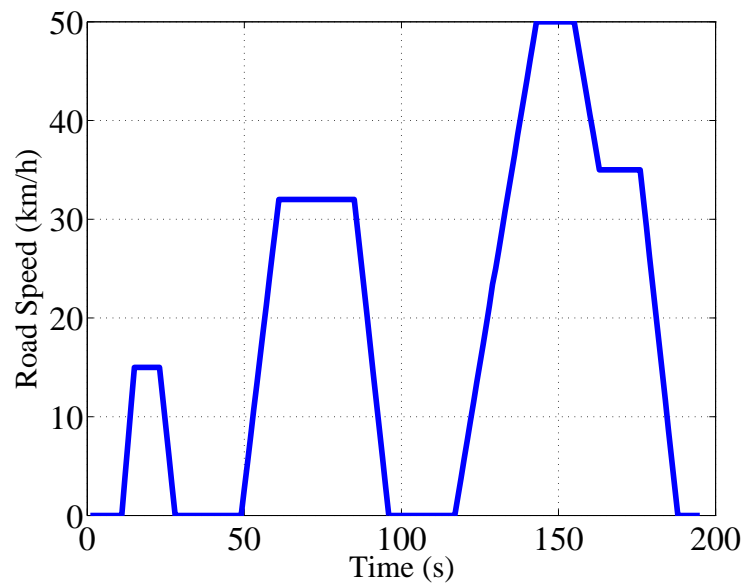


Figure 3.10: Drive cycle ECE





## Chapter 4

# Energy Efficiency Improvement in Salient Permanent Magnet Synchronous Machines

The main source of energy losses in an electric motor is the copper and the core losses. Depending on the control strategy, we can get different losses and consequently different efficiencies. The main objective of a motor controller is to obtain a certain speed at a certain torque. A secondary objective could be to maximize the torque per ampere used, or to minimize the total copper and core losses. The former is called Maximum Torque Per Ampere and the latter, is here referred to loss minimization strategy. There are some more basic strategies that simply ignore these secondary requirements and only satisfies the primary requirement of torque and speed references.

In order to control the speed of an electric motor, a speed controller is needed to receive the speed reference and compare it with the actual speed. Then it transforms it to a torque reference which is used by the current controller. A current vector controller for an electric motor will require d-q current references and compares them with the actual d-q currents. Then it will provide the voltage references for the motor. However the torque reference needs to be related to the current references. In a non-salient PMSM this can be achieved easily since torque is only related to the q-current. However in a salient PMSM, the torque is related to both the d-current and the q-current as it was shown in (2.12). There are different ways to relate the torque references to the d-q currents on basis of the secondary requirements explained in the beginning of this chapter.

## 4.1 Zero d-current control strategy

This is perhaps the easiest way to solve the problem. By simply putting the d-current to zero, torque becomes dependent on the q-current. As a result, (2.12) turns into

$$T_e = \frac{3}{2}p(\Psi_m I_{oq}) \quad (4.1)$$

So the current references will be

$$I_{dref} = 0 \quad (4.2)$$

$$I_{qref} = \frac{2T_e}{3p\Psi_m} \quad (4.3)$$

In surface mounted PMSMs, where  $L_d$  and  $L_q$  are equal it is sufficient to use zero d-current control strategy but in other PMSMs zero d-current control strategy is far from good.

It is worth mentioning that it is actually  $I_d$  and  $I_q$  which are controlled and not the  $I_{od}$  and  $I_{oq}$ . So already from the beginning we are introducing an error. This method neither guarantees the maximum torque per ampere nor provides the lowest losses.

## 4.2 Maximum torque per ampere control strategy

In this strategy d and q current references are extracted using the equations for an ideal PMSM model without core loss in order to find the maximum torque for a given current.

### 4.2.1 Extraction of ideal current vector of PMSM

In order to work easier with the mathematical expression, the equations can be stated with respect to an angle called  $\alpha$  instead of  $I_d$  and  $I_q$ .  $\alpha$  is the angle between  $I_d$  and  $I_q$ . So  $I_{sq}$  and  $I_{sd}$  are rewritten as

$$I_{sq} = I_a \cos(\alpha) \quad (4.4)$$

$$I_{sd} = I_a \sin(\alpha) \quad (4.5)$$

where  $I_a$  is the current magnitude vector. Now the torque equation can be rewritten as

$$T_e = \frac{3}{2}p[\Psi_m I_a \cos(\alpha) + (L_d - L_q) I_a I_a \cos(\alpha) \sin(\alpha)] \quad (4.6)$$

which also can be expressed as

$$T_e = \frac{3}{2}p[\Psi_m I_a \cos(\alpha) + \frac{1}{2}(L_d - L_q) I_a^2 \sin(2\alpha)] \quad (4.7)$$

$$\frac{dT_e}{d\alpha} = \frac{3}{2}p[-\Psi_m I_a \sin(\alpha) + (L_d - L_q) I_a^2 \cos(2\alpha)] \quad (4.8)$$

By expanding the  $\cos(2\alpha)$ -term the expression becomes

$$\frac{dT_e}{d\alpha} = \frac{3}{2}p[-\Psi_m I_a \sin(\alpha) + (L_d - L_q) I_a^2 \{1 - 2\sin^2(\alpha)\}] \quad (4.9)$$

This is a second order equation, and by putting the derivative to 0, the following expression is obtained

$$0 = -\Psi_m I_a \sin(\alpha) + (L_d - L_q) I_a^2 - 2(L_d - L_q) I_a^2 \sin^2(\alpha) \quad (4.10)$$

by changing signs

$$0 = \Psi_m I_a \sin(\alpha) - (L_d - L_q) I_a^2 + 2(L_d - L_q) I_a^2 \sin^2(\alpha) \quad (4.11)$$

putting it into the form of a second-order equation gives

$$0 = \sin^2(\alpha) + \frac{\Psi_m I_a}{2(L_d - L_q) I_a^2} \sin(\alpha) - \frac{1}{2} \quad (4.12)$$

removing  $i_a$

$$0 = \sin^2(\alpha) + \frac{\Psi_m}{2(L_d - L_q) I_a} \sin(\alpha) - \frac{1}{2} \quad (4.13)$$

which gives the solution

$$\sin(\alpha) = -\frac{\Psi_m}{4(L_d - L_q)I_a} \pm \sqrt{\frac{\Psi_m^2}{16(L_d - L_q)^2 I_a^2} + \frac{1}{2}} \quad (4.14)$$

of which it is the second solution that is the valid one.

$$\sin(\alpha) = -\frac{\Psi_m}{4(L_d - L_q)I_a} - \sqrt{\frac{\Psi_m^2}{16(L_d - L_q)^2 I_a^2} + \frac{1}{2}} \quad (4.15)$$

The ideal current vector can be used as a good guess for calculation of loss and efficiency map in the motor. However it cannot guarantee the maximum efficiency since the maximum torque per ampere is derived from the ideal model of the machine. Besides, the maximum torque per ampere strategy cannot lead us to find the suitable  $I_{sd}$  and  $I_{sq}$  in the field weakening area.

### 4.3 Loss minimization strategy

The aim of the current vector control method presented in this Section, is to minimize the total electrical losses in the motor. This can be achieved by minimizing both core and copper losses for a given torque reference. However, in a practical solution, it is important that the method fulfills all constraints and includes all the losses.

The PMSM model shown in Fig. 2.1 can be used to find the current vectors which can satisfy all current and voltage constraints while keeping all electrical losses minimal with the help of non-linear programming.

#### 4.3.1 Non-linear programming

A problem needs to be solved by non-linear programming when the function which is supposed to be optimized is at least quadratic and more and the constraints to this functions are not linear. If all constraints were linear, quadratic or polynomial programming can be used. The main purpose of the optimization is to minimize the target function  $f(x)$ .

$$\min f(x)$$

with the following constraints

- $A \cdot X = B$  Linear equality  
 $C \cdot X \leq D$  Linear non-equality  
 $E(X) = 0$  Non-linear equality  
 $F(X) \leq 0$  Non-linear non-equality

The target function  $f(x)$  consists of the copper losses and core losses which can be introduced as,

$$f(x) = P_{core} + P_{copper} = R_s(I_{sd}^2 + I_{sq}^2) + R_c(I_{sd} - I_{od})^2 + (I_{sq} - I_{oq})^2 \quad (4.16)$$

The state matrix  $X$  is chosen to be

$$X = [ I_{od} \ I_{oq} \ I_{sd} \ I_{sq} \ U_{sd} \ U_{sq} ]^T$$

The relations between the states can be represented by the linear equations in matrix  $A$  and  $B$  or the non linear equations in matrix  $E$ . Thus, the equivalent circuit equations will be rewritten for all four loops in the d and q equivalent circuit which was shown in Fig. 2.1.

$$-R_c I_{od} - R_c I_{sd} - \omega_r L_q I_{oq} = 0 \quad (4.17)$$

$$-R_c I_{oq} - R_c I_{sq} - \omega_r L_d I_{od} = 0 \quad (4.18)$$

$$R_c I_{od} - (R_s + R_c) I_{sd} - U_{sd} = 0 \quad (4.19)$$

$$R_c I_{oq} - (R_s + R_c) I_{sq} - U_{sq} = 0 \quad (4.20)$$

All the above equations are linear hence they can be included in the  $A$  and  $B$  matrixes.

$$A = \begin{bmatrix} -R_c & \omega_r L_q & R_c & 0 & 0 & 0 \\ -\omega_r L_d & -R_c & 0 & -R_c & 0 & 0 \\ R_c & 0 & -(R_c + R_s) & 0 & 1 & 0 \\ 0 & -R_c & 0 & -(R_c + R_s) & 0 & 1 \end{bmatrix}$$

$$B = [ 0 \ \omega_r \Psi_m \ 0 \ 0 ]$$

Equality equations are vital in order to decrease the degree of freedom for the optimization and it can also make the optimization faster. All constraints between the states should be represented in the linear and non linear non-equalities in matrix  $C, D$  and  $F$ . In this case, the constraints can be specified so that the optimization is done in motoring mode.

$$E(X) = [ T_{ref} - \frac{3}{2}p(\Psi_m I_{oq} + (L_d - L_q)I_{od}I_{oq}) ]$$

$$F(X) = \begin{bmatrix} -U_{max} + \sqrt{U_{sd}^2 + U_{sq}^2} \\ -I_{max} + \sqrt{I_{sd}^2 + I_{sq}^2} \\ -\sqrt{I_{sd}^2 + I_{sq}^2} \end{bmatrix}$$

The main constraints which are assigned in this algorithm are maximum voltage and current limits of the machine. Besides, the constraints can be defined so that the results are obtained for both motoring and generating mode.

## 4.4 Comparison of different control strategies

The machine with the specifications described in Section 3.1 is used to compare the different control strategies in this paper.

### 4.4.1 Comparison of different control strategies for an ideal machine without core loss

In this section an ideal PMSM with no core loss is selected to compare the current vectors provided by the MTPA strategy and the proposed nonlinear loss minimization strategy. The efficiency map achieved by both methods is shown in Fig. 4.1. It can be seen that the current vectors derived by the loss minimization optimization method are identical to the ones obtained using the MTPA strategy.

This is due to the fact that the MTPA automatically provides the minimum losses if the machine has no core losses. So the only controllable loss is the copper losses and it is minimized by maximizing the torque for a given current magnitude.

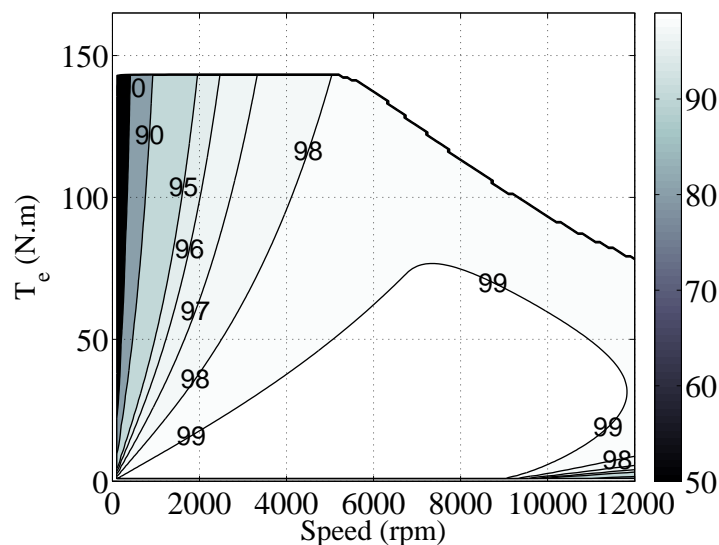


Figure 4.1: Efficiency map for minimum loss minimization control and MTPA strategies in a PMSM without core losses

#### 4.4.2 Comparison of different control strategies for a machine with core loss

In reality there is no PMSM without core loss. As a result, the ideal machine needs to include core losses. This can be done by introducing  $R_c = 40\Omega$  which in this case is a constant resistance for all operating points.  $R_c = 40\Omega$  corresponds to the core losses of the investigated machine at maximum speed.

In order to compare the loss minimization method with the MTPA, a limited operating range is chosen for a more detail investigation. A constant speed of 6000 RPM and a torque range of 10 to 40  $N \cdot m$  are chosen. Fig. 4.2 shows that the loss minimization method is providing better efficiency than the MTPA. It can also be seen in Fig. 4.3 that the loss minimization method is, as expected, providing higher copper losses in comparison with the MTPA, however it provides a lower core loss so that the total losses becomes lower in the end.

By looking at the current vector references shown in Fig. 4.4 provided by both strategies it can be seen, as was anticipated, that the loss minimization method suggests higher absolute value of the  $I_{sd}$  reference current and lower  $I_{sq}$  reference current at higher speeds so that the core losses decreases more than the amount the copper increases while the output torque is kept constant.

Now the full operating range can be compared for both strategies. The

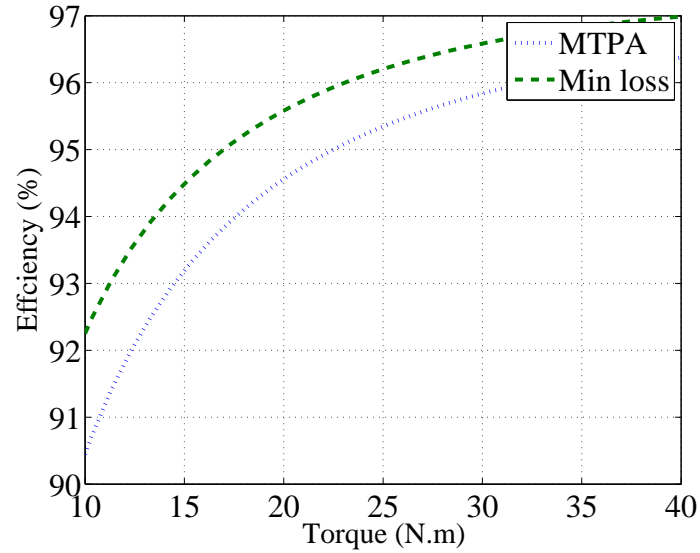


Figure 4.2: Efficiency comparison at a constant speed of 6000 rpm for a PMSM with core losses which are represented by  $R_c = 40\Omega$

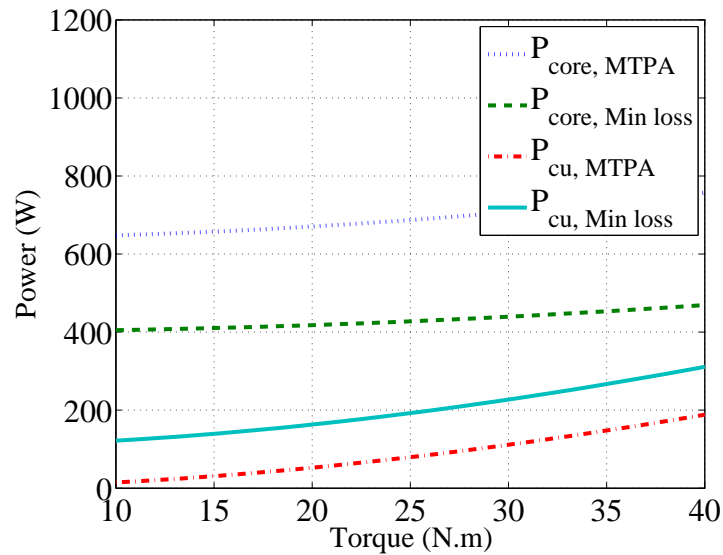


Figure 4.3: Loss comparison at a constant speed of 6000 rpm for a PMSM with core losses which are represented by  $R_c = 40\Omega$



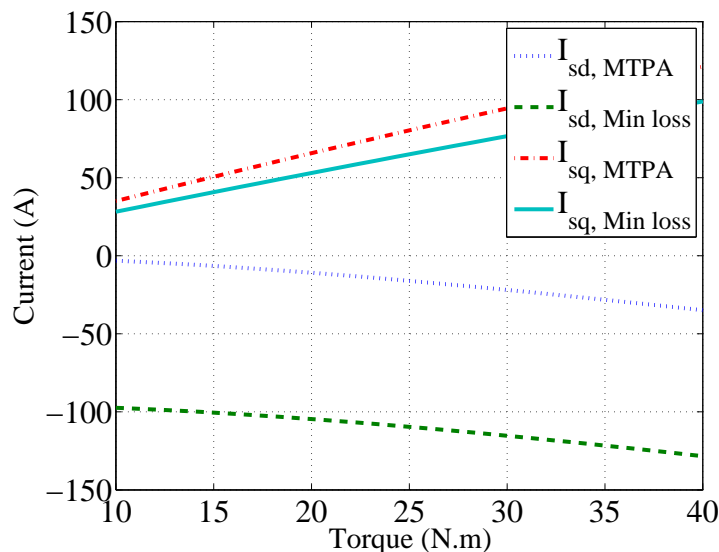


Figure 4.4: Current vector comparison at a constant speed of 6000 rpm for a PMSM with core losses which are represented by  $R_c = 40\Omega$

efficiency map is derived for both control strategies in Fig. 4.6 and 4.7. The difference between the efficiency maps (Fig. 4.8) shows the areas where the loss minimization method provided better efficiency than the MTPA. The discontinuity in the efficiency map of the MTPA (Fig. 4.6) is due to the change of method from MTPA to constant maximum voltage operation. The MTPA strategy doesn't include any limitation of the output voltage. So once the maximum voltage is reached, the voltage reference magnitude are kept constant and current vectors are calculated based on the equations provided in (2.6) to (2.12). It can be seen that the loss minimization method provides a better efficiency in comparison with MTPA, especially at higher speeds.

The corresponding  $I_{sd}$  and  $I_{sq}$  currents for both strategies in the entire operating range are shown in Fig. 4.5.

Consequently the differences between the copper losses, core losses and the total losses are shown in Fig. 4.9 to 4.11.

#### 4.4.3 Implementation of a variable $R_c$ in loss minimization optimization method

Since the core losses of an electric machine varies through the electric frequency, it would be favorable that the loss minimization method use a variable  $R_c$  to further improve the modeling and the optimization result.

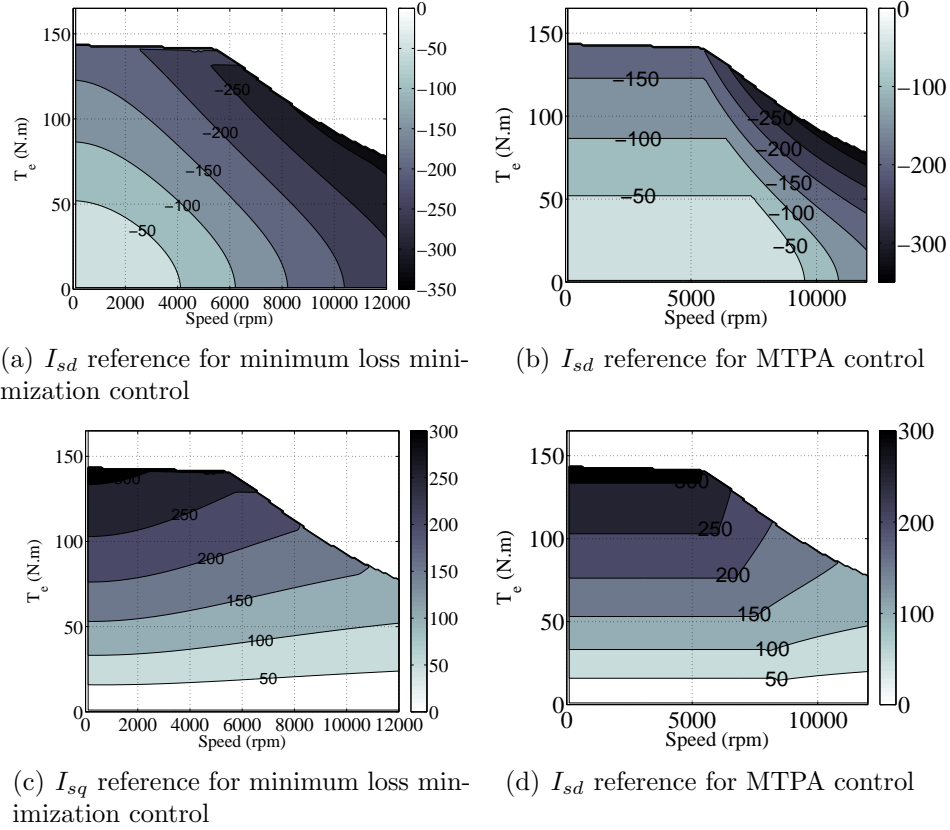


Figure 4.5:  $I_{dq}$  reference for current vectors for minimum loss minimization and MTPA control strategies in a PMSM with core losses

The efficiency maps for the loss minimization method for the machine with a variable  $R_c$  is shown in Fig. 4.12. It can be noted that the difference compared to Fig. 4.7 where a constant  $R_c$  was used is not substantial. However it provides a more realistic model especially in the low speed low torque region.

#### 4.4.4 Comparison of different drive cycles in simulation of an electric vehicle with nonlinear loss minimization strategy

The vehicle explained in Chapter 2 is used in the ECE and US06 drive cycles and the resulting loss differences due to the control strategy is shown in Fig. 4.13 and Fig. 4.14 respectively.

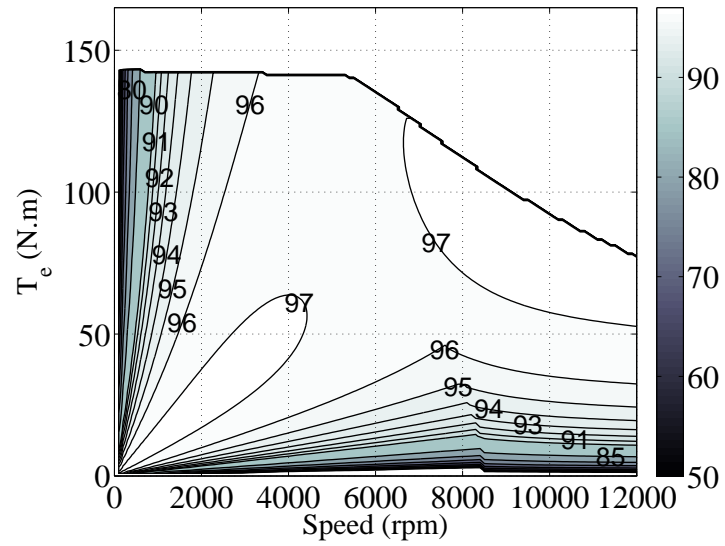


Figure 4.6: Efficiency map for MTPA strategy in a PMSM with core losses

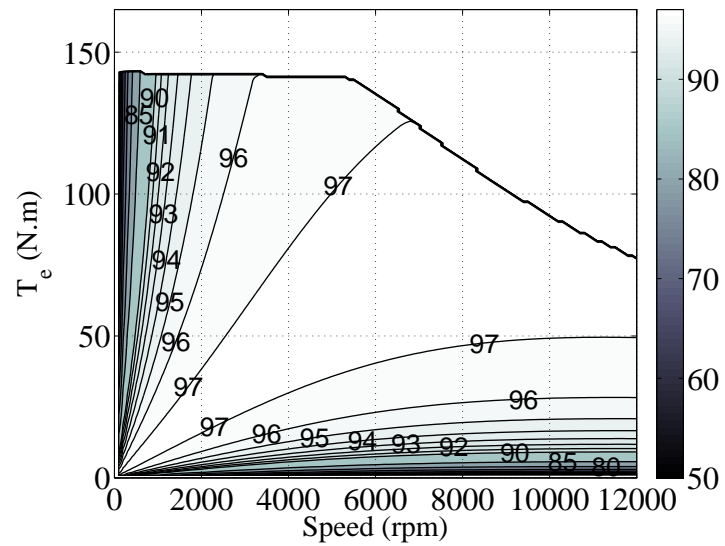


Figure 4.7: Efficiency map for minimum loss minimization control strategy in a PMSM with core losses

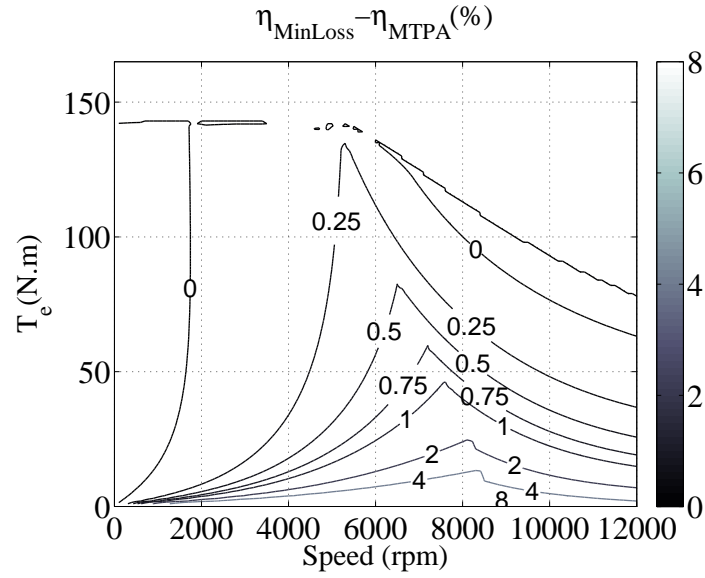


Figure 4.8: Efficiency map difference between the minimum loss minimization control MTPA strategies in a PMSM with core losses

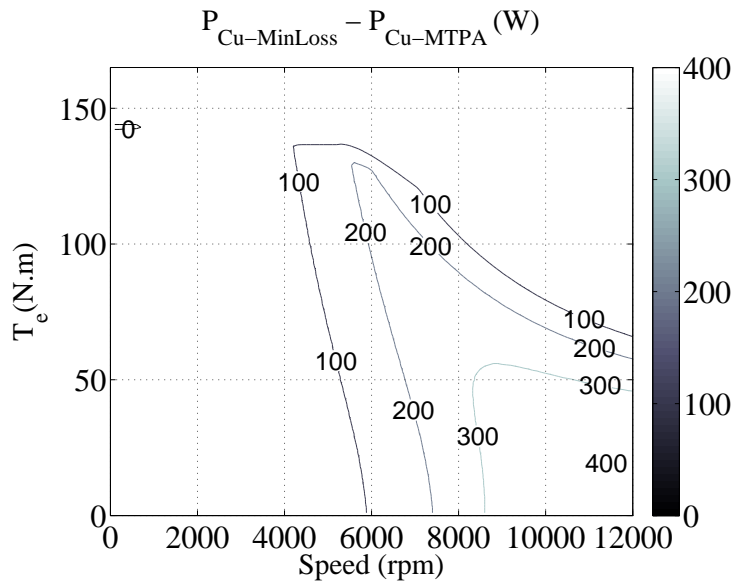


Figure 4.9: Copper loss map difference between the minimum loss minimization and MTPA control strategies

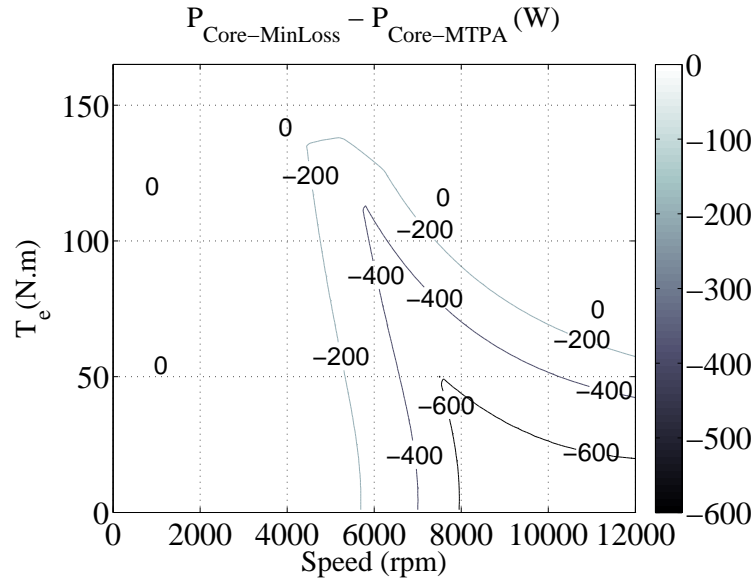


Figure 4.10: Core loss map difference between the minimum loss minimization and MTPA control strategies

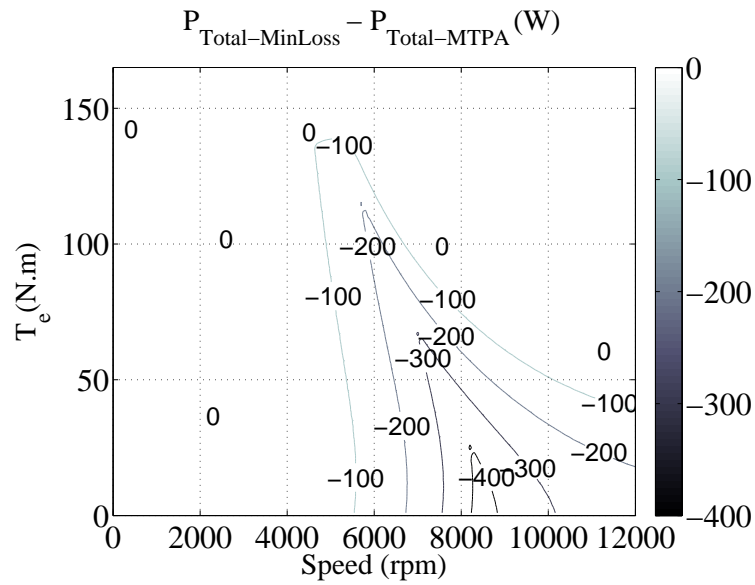


Figure 4.11: Total loss map difference between the minimum loss minimization and MTPA control strategies

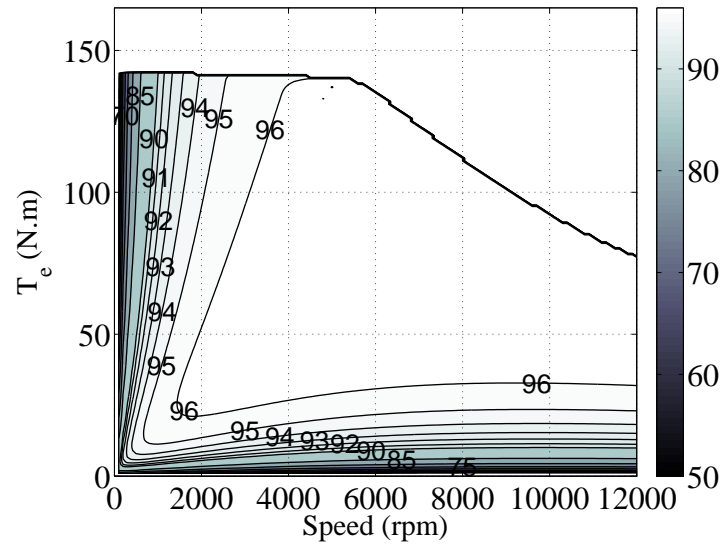


Figure 4.12: Efficiency map for minimum loss minimization control strategy in a PMSM with core losses caused by introducing a variable  $R_c$

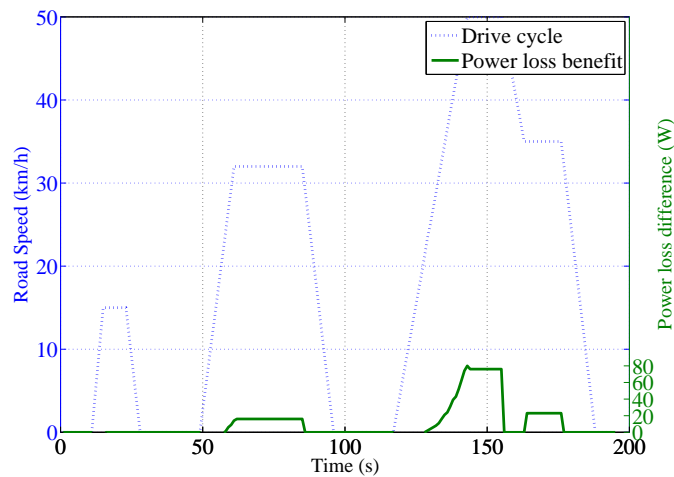


Figure 4.13: Torque-Speed characterization in ECE drive cycle

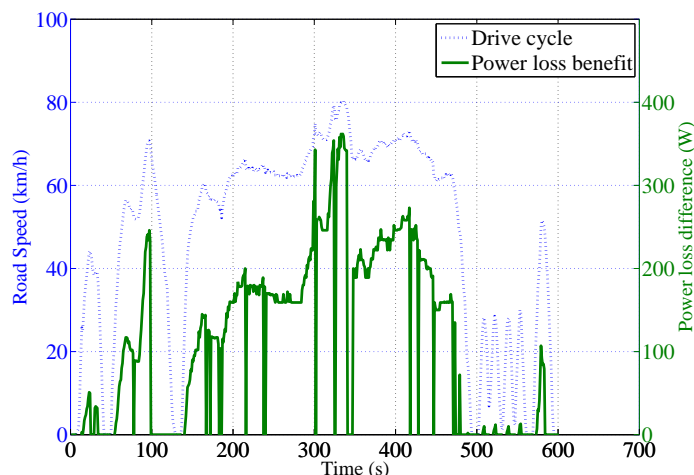


Figure 4.14: Torque-Speed characterization in US06 drive cycle

Table 4.1: Energy loss decrease due to the use of loss minimization optimization method over MTPA and the percentage of energy loss decrease over the total energy required by different drive cycles

Drive cycle	Energy loss decrease (kJ)	Percentage (%)
EUDC	73.9	1.69
ECE	2	0.37
NEDC(ECE+EUDC)	75.9	1.54
US06	66.1	1.46

It can be seen that at higher speeds, the benefit of the proposed loss minimization method is more pronounced as it was expected. It is due to the fact that the loss minimization method takes into account the core losses which are higher at higher speeds.

The average power loss decrease in each drive cycle is shown in Table 4.1. The results show that the efficiency is increased in the whole operating region, in particular in the high-speed region, where an improvement of up to 8% can be achieved. This method is simulated for a PMSM in a vehicle for the NEDC (ECE+EUDC) and US06 driving cycles. The loss minimization control strategy provided 1.54% less loss compared to the MTPA method in NEDC drive cycle.





# Chapter 5

## System Level Efficiency Analysis of using different components and voltage levels

In this chapter, different inverter solutions such as using semiconductor components with different materials or different reverse blocking voltage levels are evaluated for a vehicle propulsion inverter. Furthermore the energy efficiency consequence of using a controllable dc-link for the propulsion inverter in order to minimize the total drive system losses is studied.

The investigations are based on efficiency calculation of the vehicle explained in Section 3.5 for various drive cycles discussed in Section 3.6. The vehicle is assumed to be equipped with the electric machine presented in Section 3.1.1, the battery specified in Section 3.4 and an inverter with various semiconductor components. The loss model of the inverter is calculated based on the approximate switching loss model derived in Section 2.2.2 and the conduction loss model discussed in Section 2.2.1.

The scenarios to be investigated are

- Section 5.1 : Effect of using a SiC diode in a 600 V dc-link system
- Section 5.2 : Effect of changing the dc-link voltage level from 400 V to 800 V
- Section 5.3 : Effect of using a SiC MOSFET in a 1200 V dc-link system
- Section 5.4 : Effect of over-dimensioning the semiconductor components
- Section 5.5 : Effect of using a variable dc-link voltage for the propulsion inverter

The semiconductor components chosen for different studies in this section are found in Section 3.2. In order to have fair comparisons, some criteria have been set for choosing the components. The components are chosen due to their low losses in their own semiconductor material, class or voltage level. Besides, the components chosen for each investigation, have similar power levels. In case the desired rated module is not available for a component, several of the same components are bundled in parallel and are treated as one module.

## 5.1 Silicon Carbide Schottky freewheeling diode instead of a Silicon pn diode

Schottky diodes in general have relatively lower losses than pn diode, however, they withstand lower breakdown voltages. SiC Schottky diodes can provide both high breakdown voltages and lower losses. As a result they can be considered as an alternative to ordinary freewheeling diodes. In this section the energy efficiency consequence of choosing such a diode over an ordinary silicon diode is evaluated.

In this section, the chosen modules for the inverter are

- Setup 1: A 600 V silicon IGBT module with a built-in pn diode (FS600R07A2E3) in a 400 V dc-link system
- Setup 2: A 600 V silicon IGBT module(FS600R07A2E3) with a SiC schottky diode module (SCS220AG)30X in a 400 V dc-link system

For each setup, a three phase inverter is evaluated in combination with the machine presented in Section 3.1.1.1. The conduction losses for the inverter is calculated based on the equations found in Section 2.2.1 for the entire operating region of the motor. As it can be seen in Fig. 5.1, the conduction losses for both setups are roughly the same for the most part of the operating region of the motor. However in the very high power region, the SiC schottky diode is causing more conduction losses which is mainly due it its higher on-state resistance in comparison with the original pn diode.

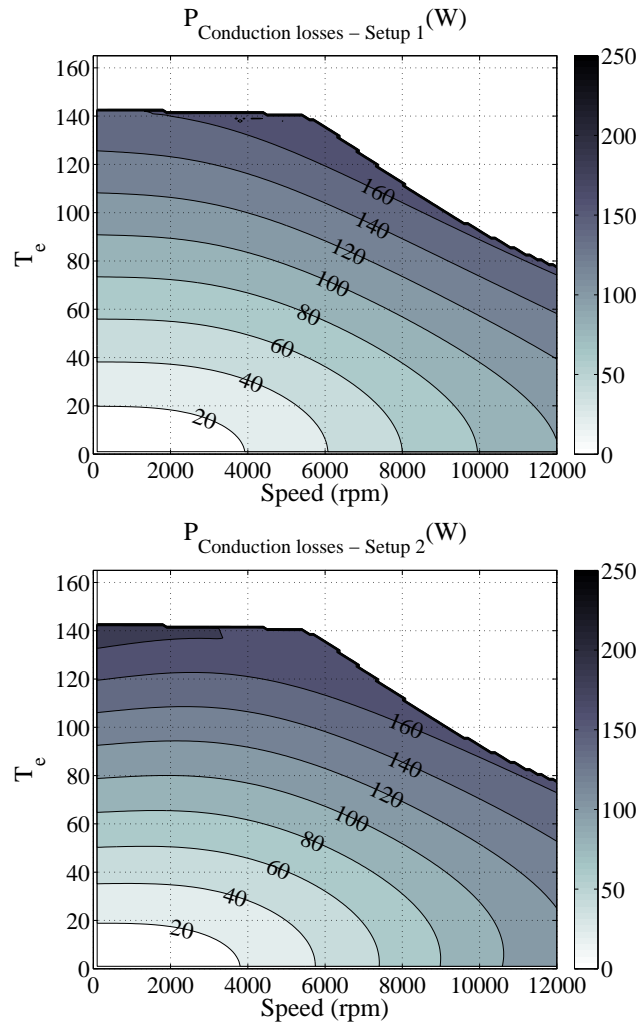


Figure 5.1: Conduction loss map for a 600V silicon IGBT(FS600R07A2E3) with a pn silicon diode versus a 600V silicon IGBT(FS600R07A2E3) with a SiC Schottky diode module(SCS220AG)30X in a 400V dc-link system

Switching losses for each inverter is calculated by the approximative switch-loss method explained in Section 2.2.2. The switching frequency is chosen to be  $10 \text{ kHz}$ . The result is shown in 5.2. It can be seen that the setup with a SiC diode has reduced switching losses in the entire operating region. This is mainly due to a significantly lower reverse recovery loss of the SiC diode.

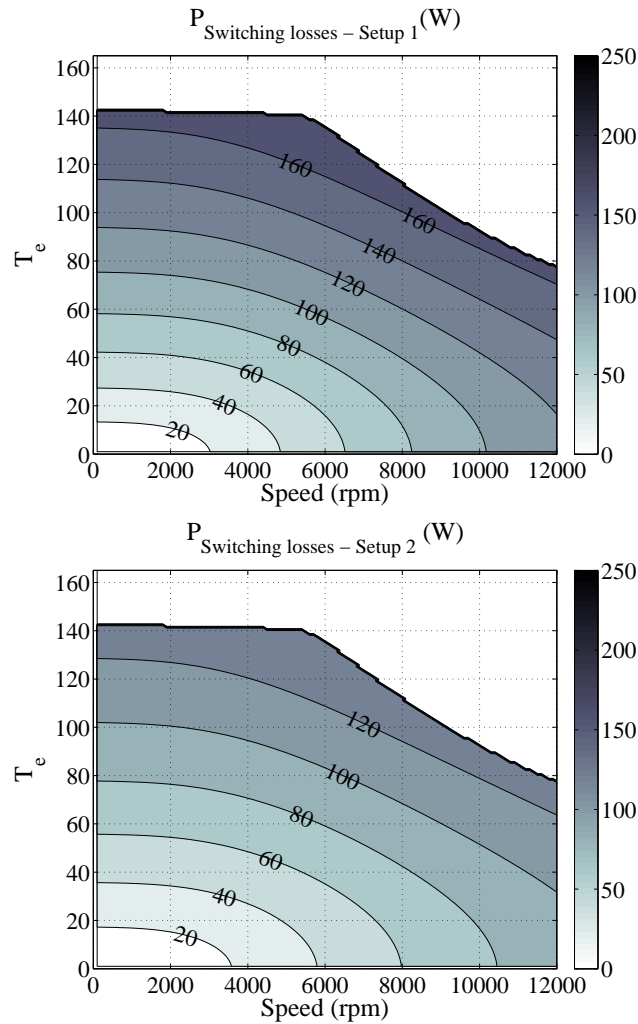


Figure 5.2: Switching loss map for a 600V silicon IGBT(FS600R07A2E3) module with a pn silicon diode versus a 600V silicon IGBT(FS600R07A2E3) module with a SiC Schottky diode module (SCS220AG)30X in a 400V dc-link system with a switching frequency of 10 kHz

The conduction and the switching losses for each setup are now added, making up the total power loss of the inverter. The total power loss for each setup are subtracted from each other and the result is shown in Fig. 5.3.

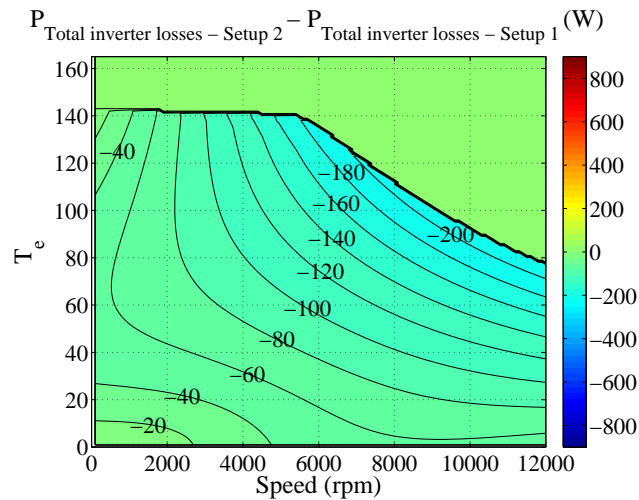


Figure 5.3: Total power loss of an inverter using a 600V silicon IGBT FS600R07A2E3 module with a SiC Schottky diode module (SCS220AG)30X minus the total power loss of the same inverter using a 600V silicon IGBT(FS600R07A2E3) with built-in pn diode in a 400V dc-link system with a switching frequency of 10 kHz

As it can be seen in Fig. 5.3, the total power loss for the setup with a SiC freewheeling diode is better in the entire region. However the main question is how much this improvement affect the energy efficiency of the inverter in various drive cycles. It can be seen in Table 5.1, that the inverter with the SiC freewheeling has an average of about half a percent improvement in drive cycle efficiency by changing the diode from silicon pn to SiC. It should also be noted that the only difference between these two setups is the freewheeling diode. As a result the inverter gate driving and other components will remain unchanged. So the only additional cost for this setup is the SiC diode themselves and they can lead to an efficiency improvement of around 0.5% in the propulsion inverter regardless of drive cycle.

Table 5.1: Drive cycle efficiency(energy losses of the inverter divided by the input power) for 'Setup 1' with a pn diode and 'Setup 2' with a SiC Schottky diode

Drive cycle	Efficiency for Setup 1(%)	Efficiency for Setup 2 (%)
EUDC	94.77	95.24
ECE	91.72	92.54
US06	93.30	93.89

## 5.2 Change of the dc-link voltage level from 400V to 800V

In this section the effect of choosing a higher dc-link voltage is investigated. The components that were used to tolerate a maximum voltage of 600V in a 400V dc-link system, are changed to 1200V component in a 800V dc-link system.

To make a fair comparison, the PMSM motor is scaled for two different voltage levels of 400V and 800V in Section 3.1.1.1. The 400V scaled motor is used to operate the inverter using the module in 'Setup 1' and the 800V scaled motor is used to operate the inverter using the module in 'Setup 2'.

- Setup 1: A 600V silicon IGBT module with built-in pn diode (FS600R07A2E3)
- Setup 2: A 1200V silicon IGBT module with built-in pn diode (CM3000EXS-24S)

Conduction loss for the both inverters is calculated based on the equations found in Section 2.2.1 for the entire operating region of the motor. As it can be seen in Fig. 5.4, the 1200V IGBT has slightly lower conduction loss in comparison with the 600V IGBT.

Switching losses for each inverter is calculated by the approximated switching loss method explained in Section 2.2.2. The switching frequency is chosen to be 10 kHz. The result is shown in 5.5. It can be seen that the switching loss in the setup with the 1200V IGBT has much higher switching loss in the entire operating region. This higher switching loss in the 1200V IGBT has canceled the benefit of lower conduction loss and the total power loss in the 1200V inverter has shown to be higher than the 600V inverter in Fig 5.6. As it is shown in Table 5.2 this results in a 0.5 % to 1.4% decrease in drive cycle efficiency.

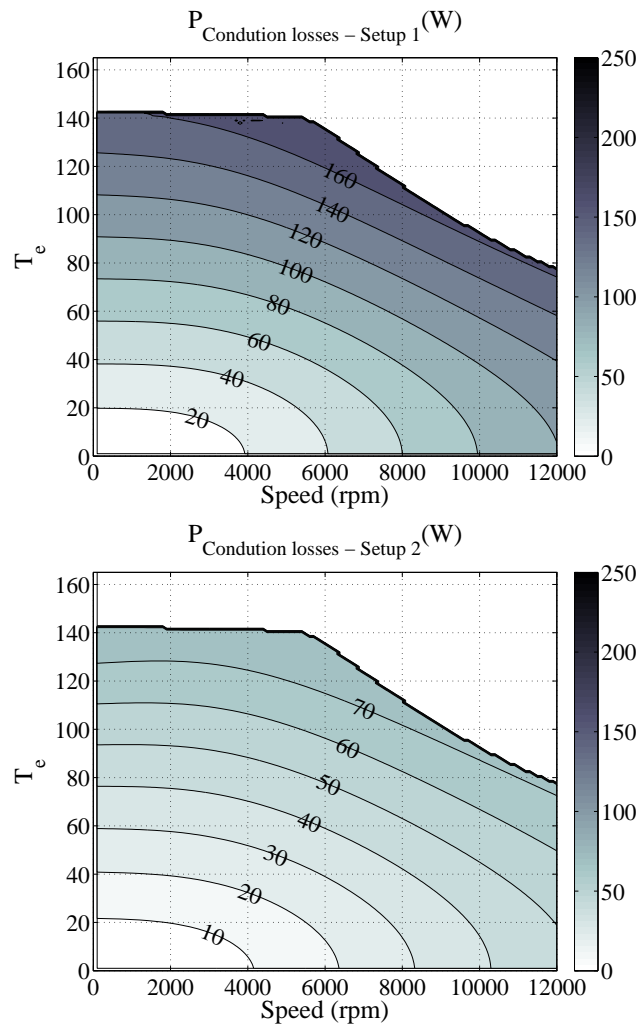


Figure 5.4: Conduction loss map for a 600V silicon IGBT(FS600R07A2E3) in a 400V dc-link system versus a 1200V silicon IGBT(CM3000EXS-24S) in a 800V dc-link system with a switching frequency of 10 kHz

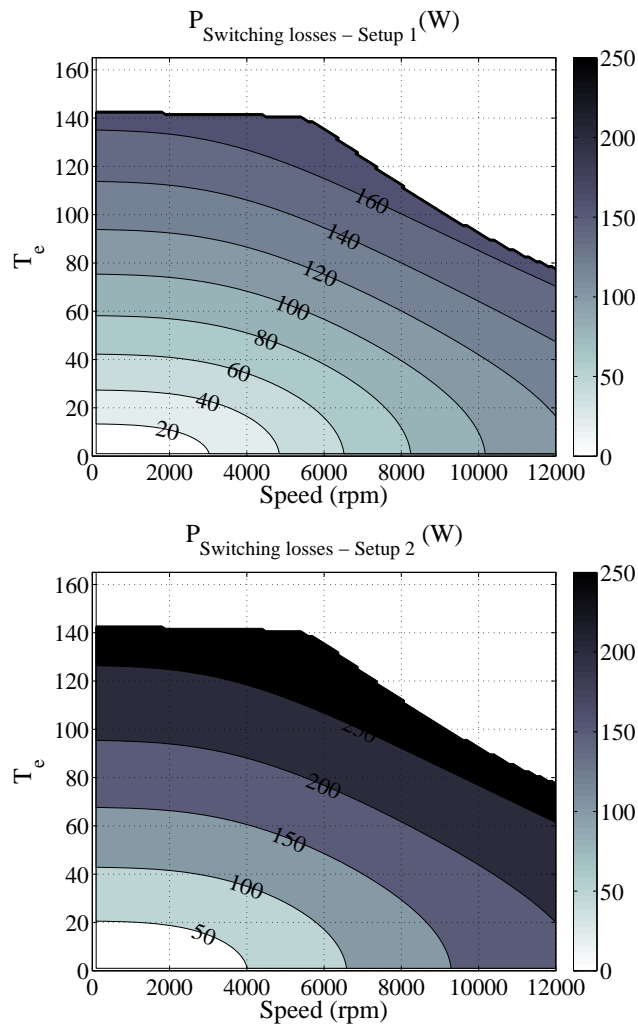


Figure 5.5: Switching loss map for a 600V silicon IGBT(FS600R07A2E3) in a 400V system versus a 1200V silicon IGBT(CM3000EXS-24S) in a 800V system with a switching frequency of 10 kHz



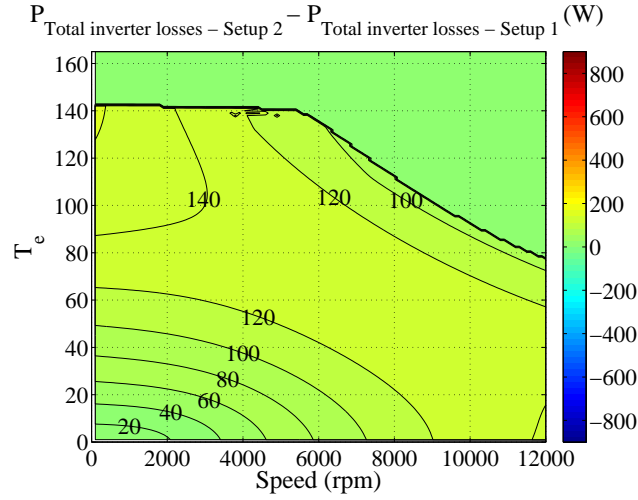


Figure 5.6: Total power loss of an inverter using a 1200V silicon IGBT(CM3000EXS-24S) minus the power loss of the same inverter using 1200V silicon IGBT(CM3000EXS-24S)

Table 5.2: Drive cycle efficiency(energy losses of the inverter divided by input power) for 'Setup 1' with a 600V IGBT and 'Setup 2' with a 1200V IGBT

Drive cycle	Efficiency for Setup 1(%)	Efficiency for Setup 2 (%)
EUDC	94.77	94.06
ECE	91.72	90.43
US06	93.30	92.35

### 5.3 Silicon Carbide MOSFET as main switching device

In this section the energy efficiency consequence of choosing a SiC MOSFET instead of an ordinary silicon IGBT is evaluated.

- Setup 1: A 1200V silicon IGBT module with built-in pn diode (CM3000EXS-24S)
- Setup 2: A 1200V SiC MOSFET module with built-in SiC diodes (SCH2080KE)10X

For each setup, a three phase inverter is evaluated in combination with the machine presented in Section 3.1.1.1. The conduction losses for the inverter is calculated based on the equations found in Section 2.2.1 for the entire operating region of the motor. As it can be seen in Fig. 5.1, conduction losses for SiC MOSFET is slightly higher than the IGBT. The difference is a bit more visible in the high power region.

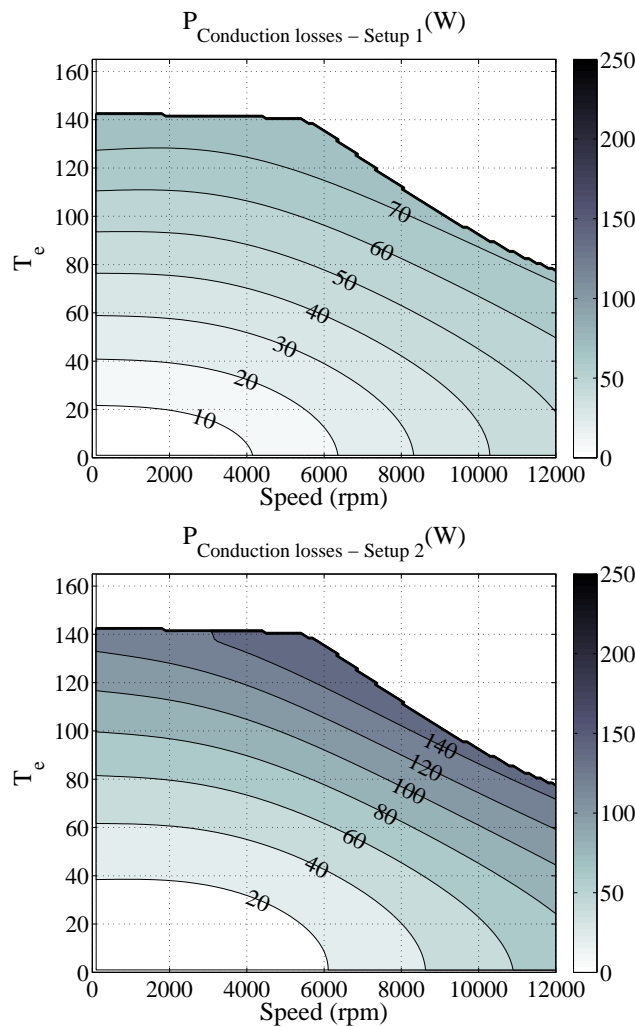


Figure 5.7: Conduction loss map for a 1200V silicon IGBT(CM3000EXS-24S) module versus a 1200V SiC MOSFET(SCH2080KE)10X module in a 800V dc-link system

Switching losses for each inverter is calculated by the approximated switching loss method explained in Section 2.2.2. The switching frequency is chosen to be  $10\text{ kHz}$ . The result is shown in 5.8. It can be seen that the setup with the SiC MOSFET has much lower switching loss in the entire operating region.

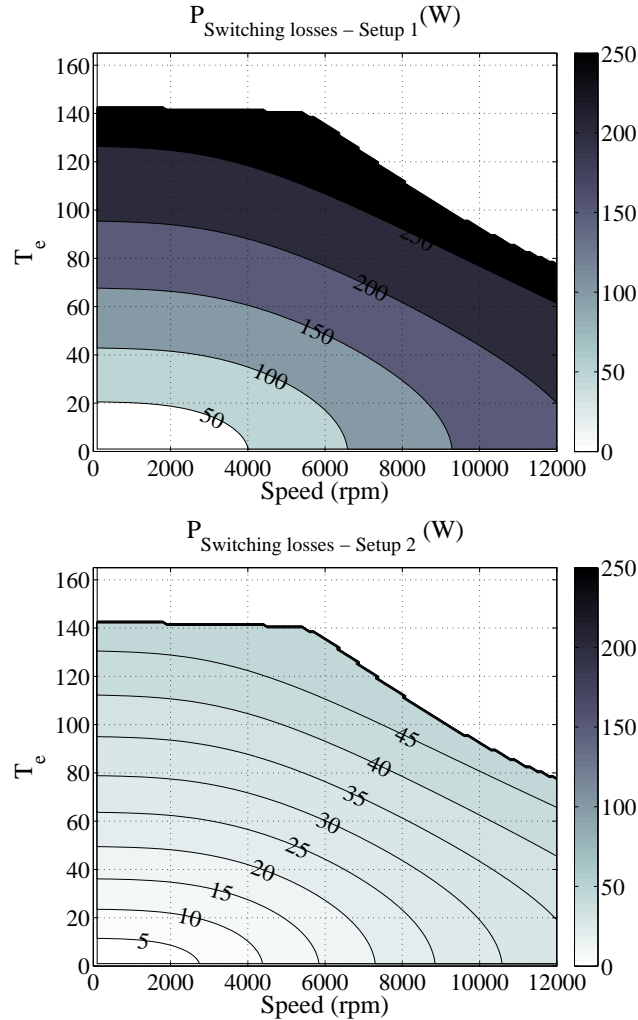


Figure 5.8: Switching loss map for a 1200V silicon IGBT(CM3000EXS-24S) module versus a 1200V SiC MOSFET(SCH2080KE)10X module in a 800V dc-link system with a switching frequency of 10 kHz

The conduction and the switching losses for each setup are added, making up the total power loss of the inverter. The total power loss for each setup are subtracted from each other and the result is shown in Fig. 5.9.

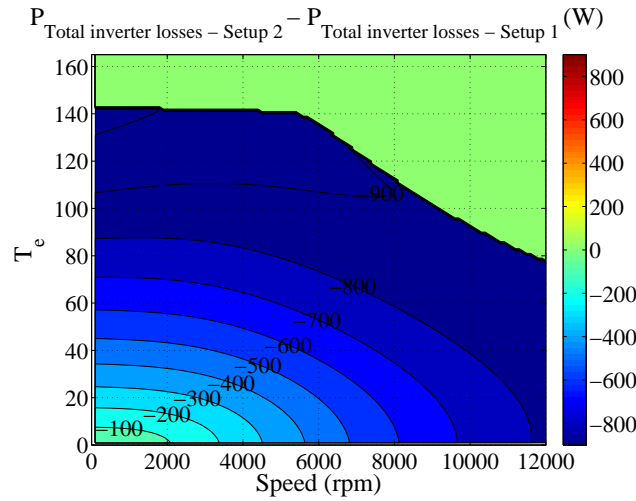


Figure 5.9: Total power loss of an inverter using a 1200V SiC MOSFET(SCH2080KE)10X module in parallel minus the total power loss of the same inverter using a 1200V silicon IGBT CM3000EXS-24S module

As it can be seen in Fig. 5.9, the total power loss for the setup with a SiC MOSFET is significantly lower than the IGBT in the entire operating region. However the main question is how much this improvement affect the inverter in various drive cycles. It can be seen in Table 5.3, that the inverter with a SiC MOSFET has on average, 4 to 6 percents improvement in drive cycle efficiency. It should also be noted that a change from a silicon IGBT to a SiC MOSFET would require a significant change in the inverter design from the gate driver to issues regarding the higher voltage and current overshoots such as EMI problems.

Table 5.3: Drive cycle efficiency(energy losses of the inverter divided by the input power) for 'Setup 1' with a silicon IGBT and 'Setup 2' with a SiC MOSFET with a switching frequency of 10 kHz

Drive cycle	Efficiency for Setup 1(%)	Efficiency for Setup 2 (%)
EUDC	94.06	97.85
ECE	90.43	97.00
US06	92.35	97.33

### 5.3.1 Effect of switching frequency on the component selection

The impact of using a SiC MOSFET instead of a silicon IGBT was shown in Section 5.3. The calculation of the switching loss was conducted for a switching frequency of 10 kHz which led to much lower switching loss in the SiC MOSFET than in the silicon IGBT. However when the switching frequency is set to 5 kHz, the total loss difference is not as much and this can be seen Fig. 5.10.

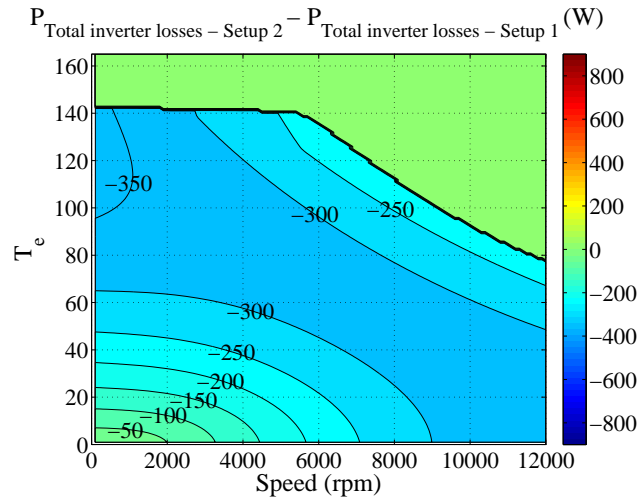


Figure 5.10: Total power loss of an inverter using a 1200V silicon IGBT CM3000EXS-24S module minus the power loss of the same inverter using a 1200V SiC MOSFET(SCH2080KE)10X module in a 800V dc-link system with a switching frequency of 5 kHz

As in it can be seen in Table 5.4, the average drive cycle efficiency for the inverter with the SiC MOSFET is still 3 percents higher than the inverter with silicon IGBT. However comparing with the case with the switching frequency of 10 kHz, shown in Table 5.3, the benefit is lower. It should also be noted that it is not preferable to decrease the switching frequency to increase the efficiency of the IGBT as it will increase the magnitude of the harmonic currents and will eventually requires bigger and more expensive filters.

Table 5.4: Drive cycle efficiency(energy losses of the inverter divided by the input power) for 'Setup 1' with a silicon IGBT and 'Setup 2' with a SiC MOSFET with a switching frequency of 5 kHz

Drive cycle	Efficiency for Setup 1(%)	Efficiency for Setup 2 (%)
EUDC	96.49	98.28
ECE	94.40	97.70
US06	95.49	97.89

## 5.4 Overdimensioning of components in the inverter

Overdimensioning of the inverter in this section, refers to the use of switching components with higher current ratings. This can be achieved by either choosing higher rated components or putting several components in parallel. The aim is to reduce the on-state resistance of the switching components to reduce the conduction loss and eventually increase the efficiency. The best outcome would be to reduce the total loss per chip area of semiconductors so much as the need for a liquid cooling of the inverter is eliminated. In this section, the previously used components are chosen to be overdimensioned.

### 5.4.1 Overdimensioned Silicon IGBT

In this section, the overdimensioned device is a silicon IGBT. The setups to be compared are

- Setup 1 : One 600V silicon IGBT module with built-in pn diode (FS600R07A2E3)
- Setup 2 : Two parallel 600V silicon IGBT modules with built-in pn diode (FS600R07A2E3)

As it can be seen in Fig. 5.11, the conduction loss is only reduced in the very high power region whereas the switching losses shown in Fig. 5.12 has remained unchanged.

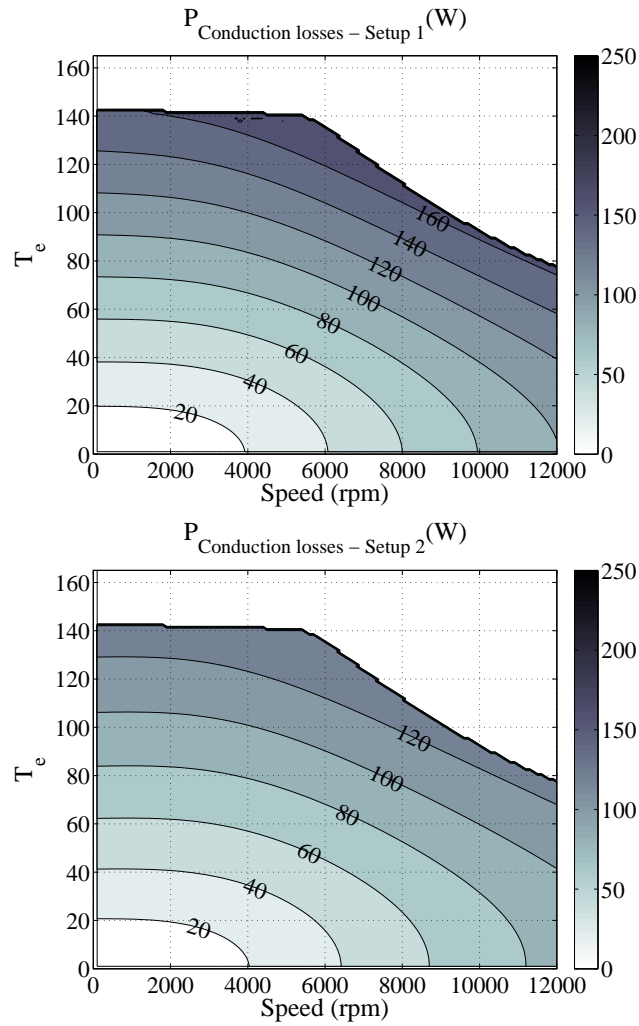


Figure 5.11: Conduction loss map for a 600V silicon IGBT(FS600R07A2E3) module versus over-dimensioned two silicon IGBT(FS600R07A2E3) module in a 400V system with a switching frequency of 10 kHz

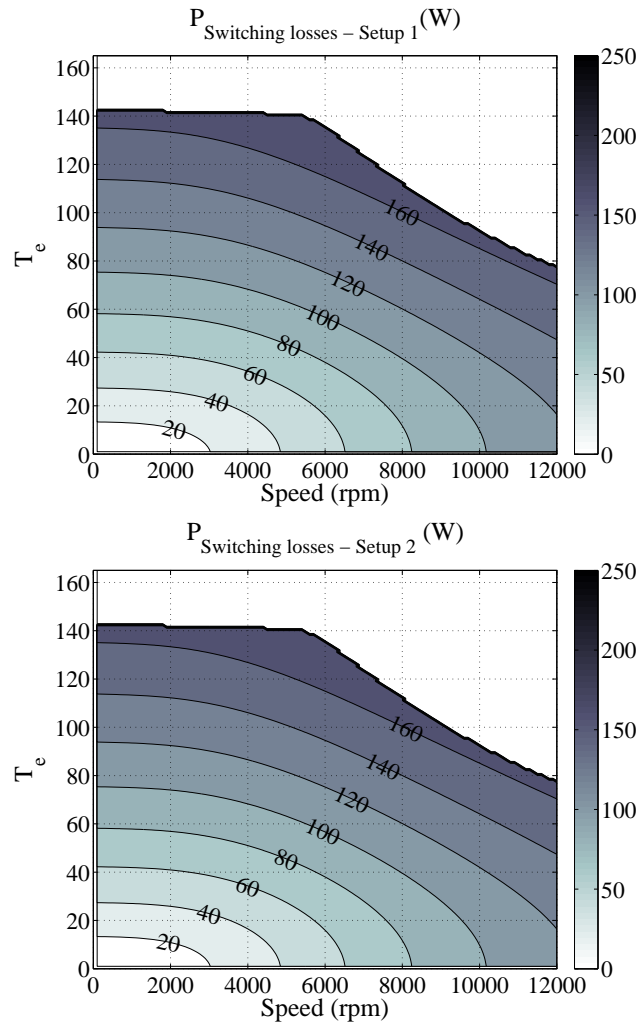


Figure 5.12: Switching loss map for a 600V silicon IGBT(FS600R07A2E3) module versus over-dimensioned two silicon IGBT(FS600R07A2E3) modules in a 400V system with a switching frequency of 10 kHz

The total power loss difference of these two setups is shown in Fig. 5.13 and the impact of using the overdimensioned IGBT on the efficiency of the drive cycle can be seen in Table 5.5. There is about 0.2% to 0.5% improvement in the total efficiency depending on the drive cycle. Considering the fact that twice as much IGBT modules were used to achieve this improvement, this seems very unlikely to be a suitable solution.



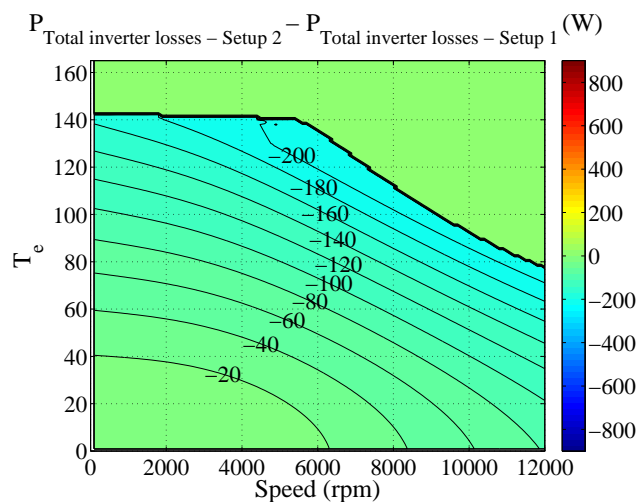


Figure 5.13: Total power loss of an inverter using a 600V silicon IGBT(FS600R07A2E3) minus the power loss of the same inverter using two 600V silicon IGBT modules (FS600R07A2E3) in a 400V dc-link system with a switching frequency of 10 kHz

Table 5.5: Drive cycle efficiency(energy losses of the inverter divided by the input power) for 'Setup 1' with a silicon IGBT and 'Setup 2' with the same component but oversized

Drive cycle	Efficiency for Setup 1(%)	Efficiency for Setup 2 (%)
EUDC	94.77	95.02
ECE	91.72	91.98
US06	93.30	93.59

## 5.4.2 Overdimensioned SiC MOSFET

In this section, the oversized device is a SiC MOSFET. The setups to be compared are

- Setup 1: A 1200V SiC MOSFET module with built-in SiC Schottky diode (SCH2080KE)10X
- Setup 2: Two parallel 1200V SiC MOSFET modules with built-in SiC Schottky diode (SCH2080KE)10X

As it can be seen in Fig. 5.14, the conduction loss is only reduced in the very high power region whereas the switching losses shown in Fig. 5.15 has remained unchanged.

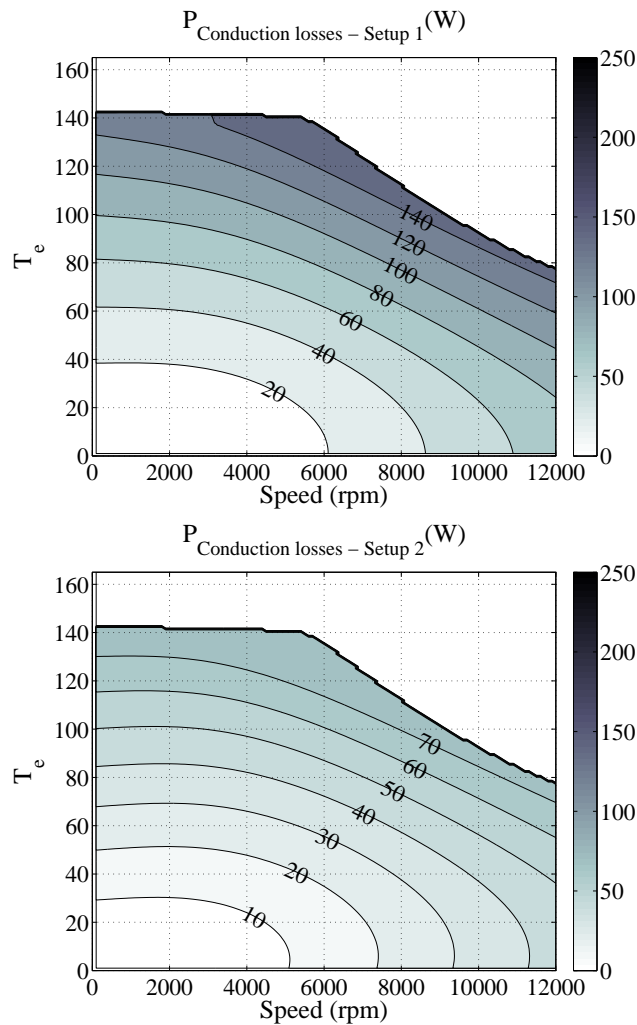


Figure 5.14: Conduction loss map for a 1200V SiC MOSFET module with built-in SiC diode (SCH2080KE)10X versus over-dimensioned two 1200V SiC MOSFET module with SiC diodes(SCH2080KE)10X in a 800V dc-link system

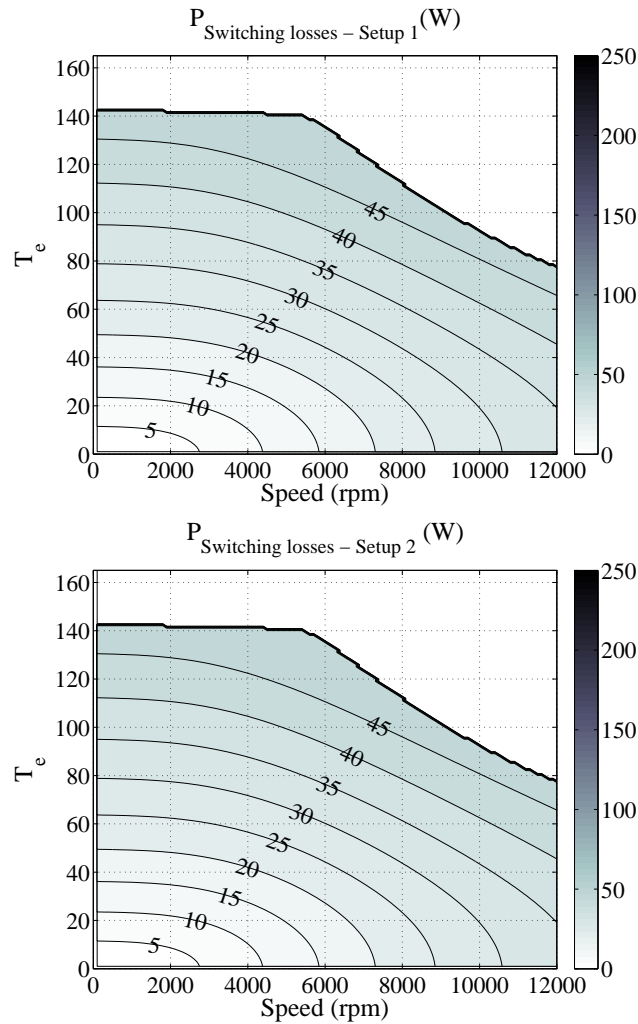


Figure 5.15: Switching loss map for a 1200V SiC MOSFET module with built in SiC diode(SCH2080KE)10X versus over-dimensioned setup with two similar modules in a 800V dc-link system with a switching frequency of 10 kHz

The differential total power loss for these setups is shown in Fig. 5.16. It shows that the losses decrease due to overdimensioning in the high power region. As it can be seen in Table 5.6, this results in about 0.5% to 0.7% improvement in the total efficiency depending on the drive cycle. This improvement is higher than in the investigating the overdimensioned IGBT.

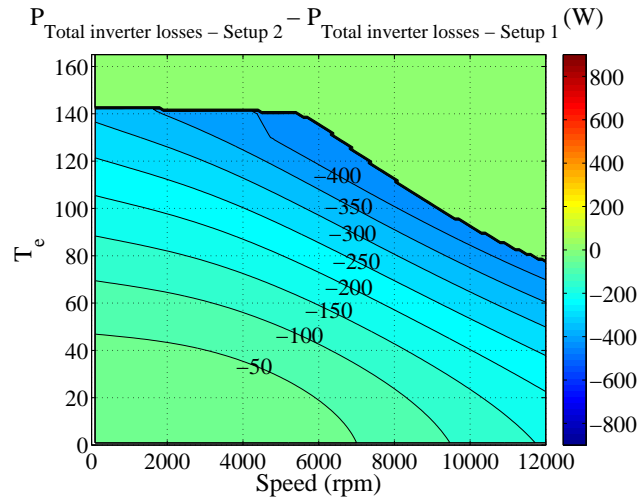


Figure 5.16: Power loss of an inverter using a 1200V SiC MOSFET module with built-in SiC diode(SCH2080KE)10X minus the power loss of the same inverter using an over-dimensioned setup with two similar modules.

Table 5.6: Drive cycle efficiency(energy losses of the inverter divided by the input power)for 'Setup 1' with a SiC MOSFET and 'Setup 2' with the same component but overdimensioned

Drive cycle	Efficiency for Setup 1(%)	Efficiency for Setup 2 (%)
EUDC	97.8	98.34
ECE	97.00	97.50
US06	97.33	97.89

## 5.5 System level efficiency analysis in a propulsion inverter with a controllable dc-link voltage

In the previous sections the dc-link voltage of the inverter was strictly constant and was chosen in accordance with the maximum allowed blocking voltage of the components. In an electric vehicle, the inverter is fed by a battery and the battery has a variable voltage. This would lead to a different loss model for the inverter which is investigated in Section 5.5.1. On the other hand, the possibility of minimizing the total motor and inverter loss by having a controllable variable dc-link voltage is also explored in Section 5.5.2.

The vehicle specified in Section 3.5, the electric motor specified in Section 3.1.1.2 and the battery specified in Section 3.4 are used for the system efficiency analysis. The inverter loss model is essentially based on the approximate loss model derived in Section 2.2.2. Based on the comparison made in Chapter 5 for different components, the SiC MOSFET module with a built-in SiC diode (SCH2080KE)10X as a prospective technology for the vehicle propulsion inverter and the silicon IGBT with a built-in pn diode (CM300EXS-24S) are chosen for the inverter.

The resulting efficiency map in three different voltage levels for the SiC MOSFET and the silicon IGBT are shown in Fig. 5.17 and 5.18 respectively.

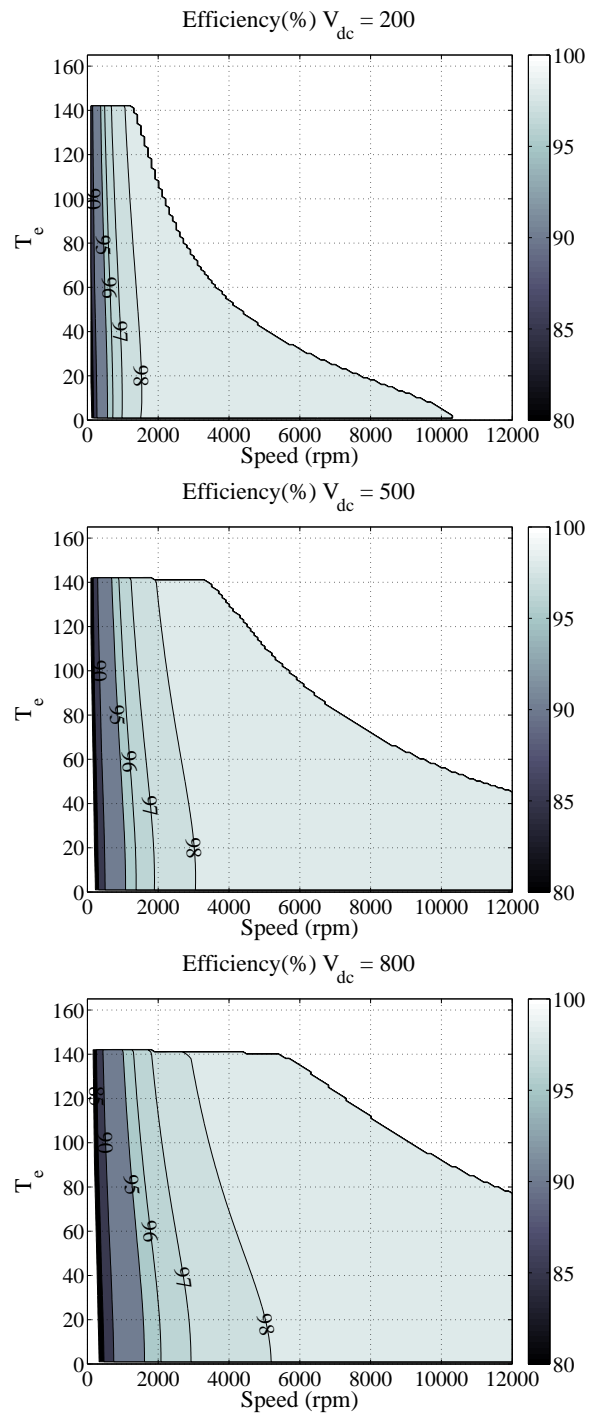


Figure 5.17: Inverter efficiency in different torque, speed and dc-link voltages using the SiC MOSFET module with built-in SiC diode(SCH2080KE)10X.

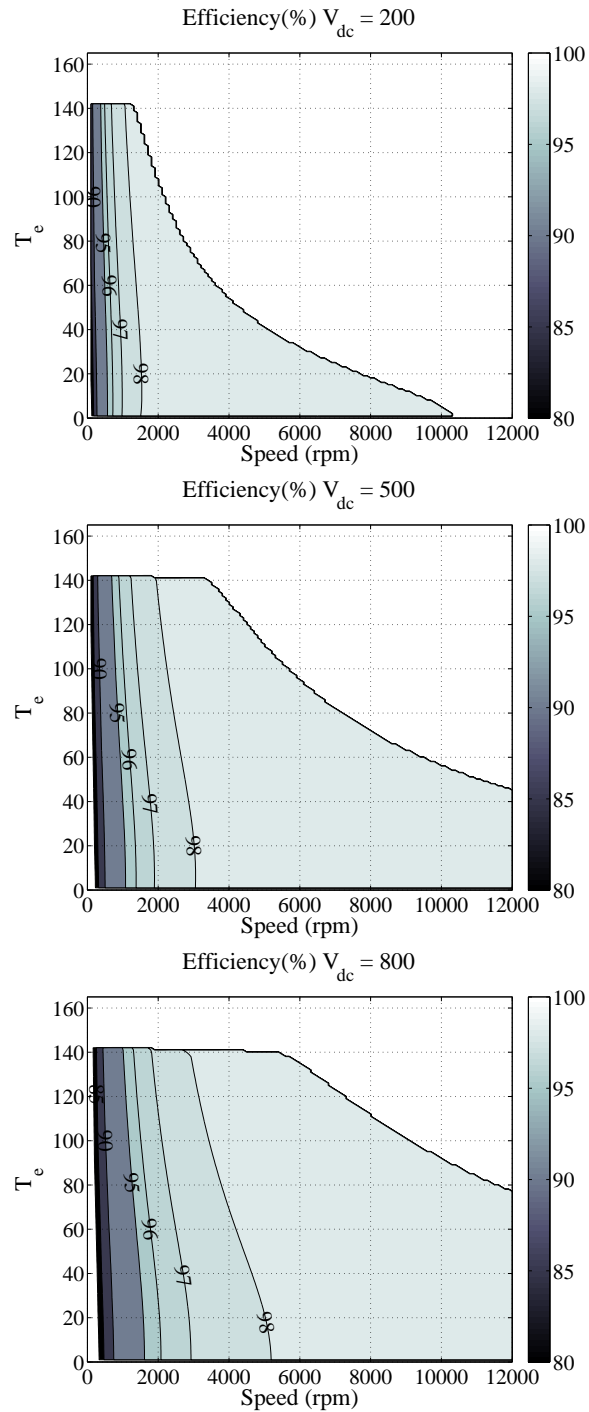


Figure 5.18: Inverter efficiency in different torque, speed and dc-link voltages using the silicon IGBT module with built-in pn diode(CM300EXS-24S).

### 5.5.1 Ordinary system without a possibility to control the dc-link voltage

In this section the vehicle presented in Section 3.5, the inverter explained in Section 3.2, the battery explained in Section 3.4 and the machine explained in Section 3.1.1.2 are used to evaluate losses on all components and on the system voltage levels for different drive cycles.

The EUDC drive cycle is run for 5 times so the battery is discharged from an 80% initial value, to a 23% value. The current and voltage of the battery as well as the SOC are shown in Fig. 5.19. The resulting instantaneous efficiency of the components for one drive cycle is shown in Fig. 5.20 All operating points during the entire drive cycle can be found in the full loss map shown in Fig. 5.21.

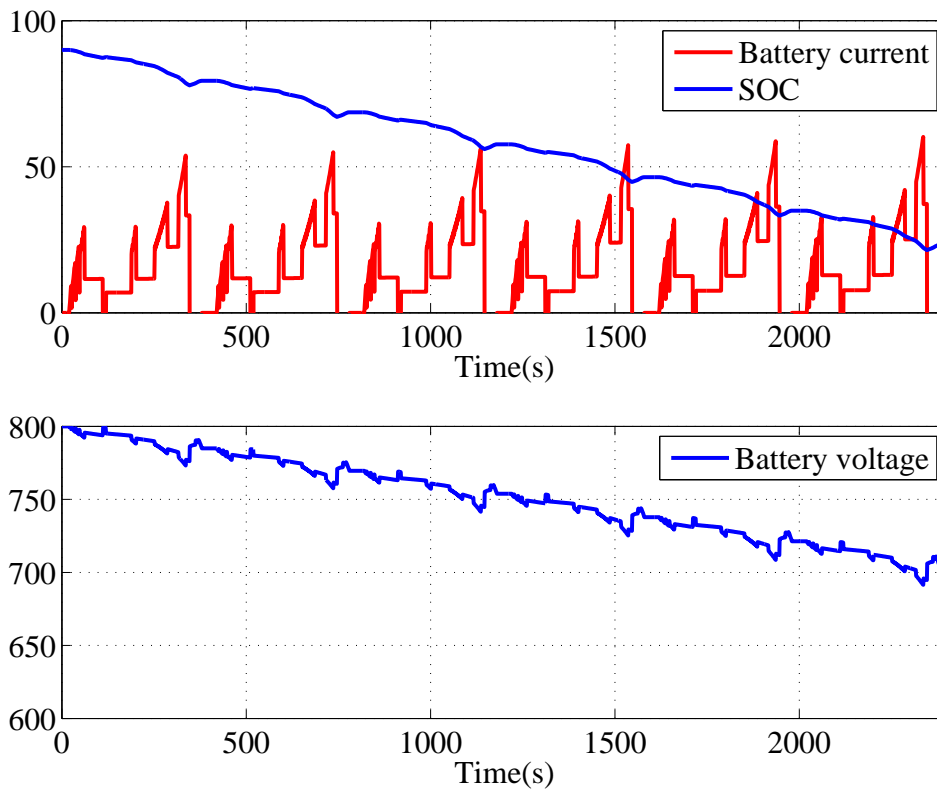


Figure 5.19: Battery current and voltage, and SOC during six consequent EUDC drive cycles



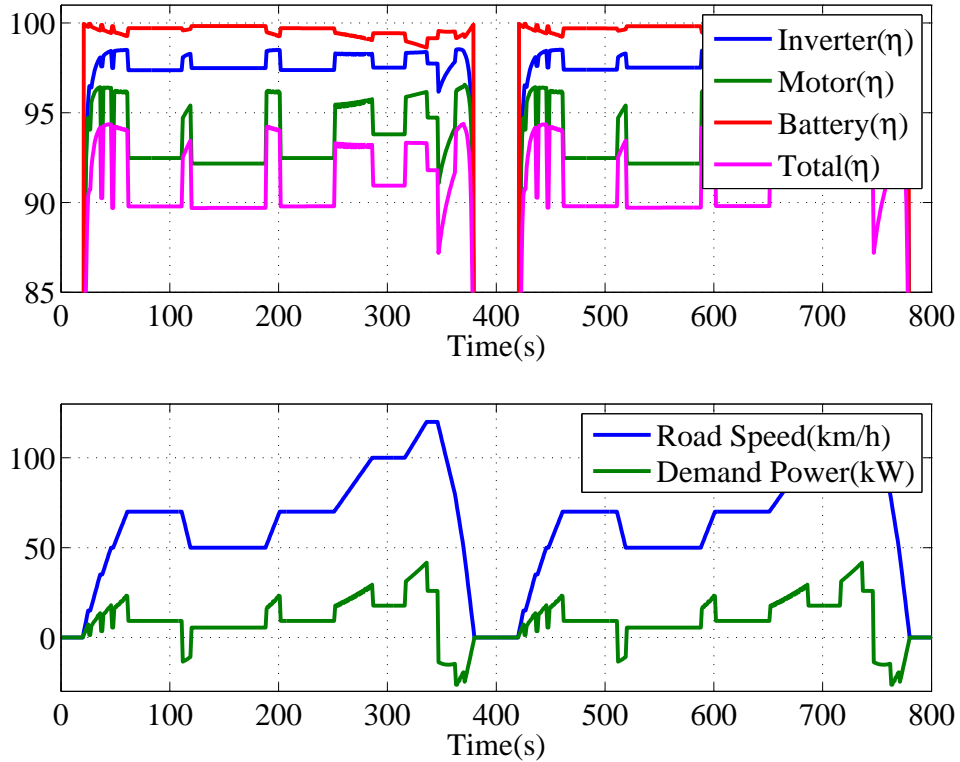


Figure 5.20: Instantaneous efficiency of different components for two consequent EUDC drive cycles

Similar experiment has been done for ECE and US06 drive cycles and the results are shown for the SiC MOSFET in Table 5.7 and the silicon IGBT in Table 5.8 .

Table 5.7: Drive cycle efficiency of components in various drive cycles without controllable dc-link voltage using the SiC based inverter

Drive cycle	Total efficiency(%)	Inverter(%)	Motor(%)	Battery(%)
EUDC(6x)	91.74	97.91	94.53	99.31
ECE(56X)	91.42	97.10	94.61	99.72
US06(6X)	90.71	97.42	93.78	99.51

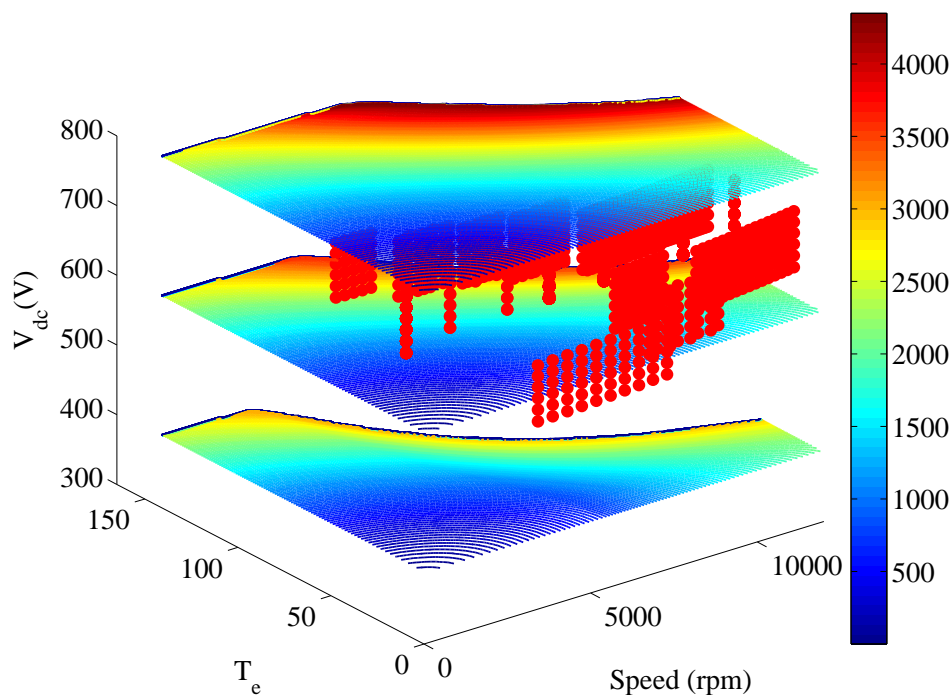


Figure 5.21: Torque - Speed - Dc-link voltage trajectory of running six consequent EUDC drive cycles with a dc-link voltage only varied by the battery, illustrated in different power loss plains

Table 5.8: Drive cycle efficiency of components in various drive cycles without controllable dc-link voltage using the silicon IGBT based inverter

Drive cycle	Total efficiency(%)	Inverter(%)	Motor(%)	Battery(%)
EUDC(6x)	88.21	94.37	94.53	99.31
ECE(56X)	85.24	90.92	94.61	99.72
US06(6X)	86.07	92.78	93.78	99.51

### 5.5.2 Ordinary system with a controlled variable dc-link voltage system

In this section, the dc-link voltage can be controlled regardless of the battery voltage. In each drive cycle and each operating point in the vehicle, the dc-link voltage which minimizes the total inverter and machine loss is chosen. The resulting instantaneous efficiency of the components for one drive cycle is shown in Fig. 5.20.

All operating points during the entire drive cycle can be found in the full loss map shown in Fig. 5.21. It can be seen in Fig. 5.21 how many operating points that have been moved to a lower voltage level to decrease the losses due to the switching losses.

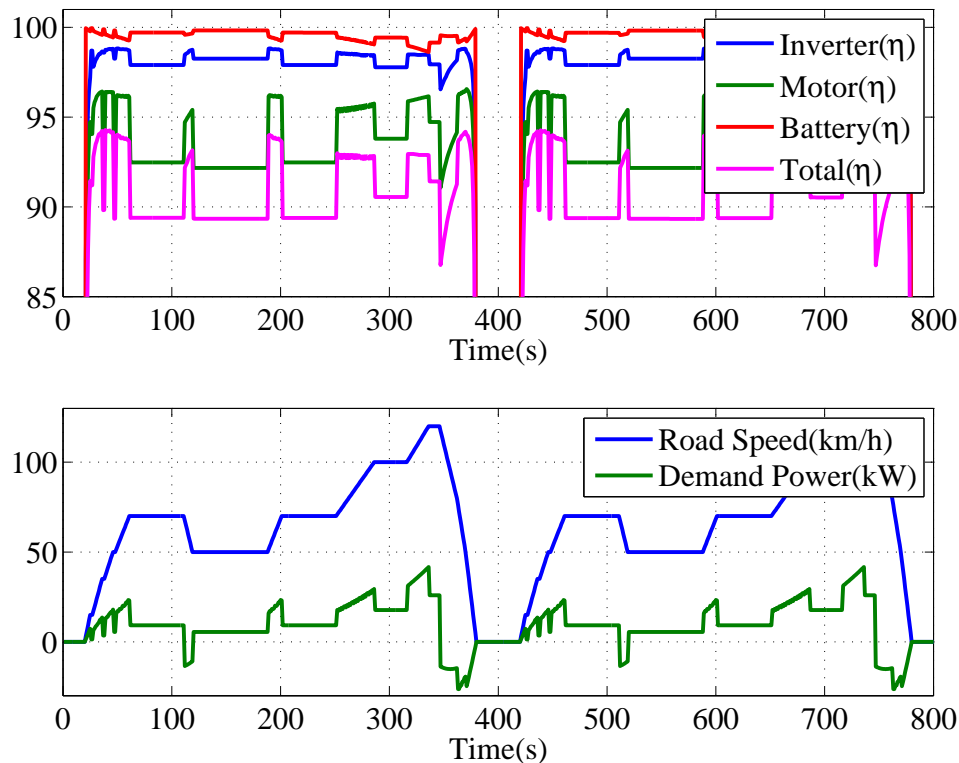


Figure 5.22: Instantaneous efficiency of different components using a controllable dc-link voltage when running two consequent EUDC drive cycles

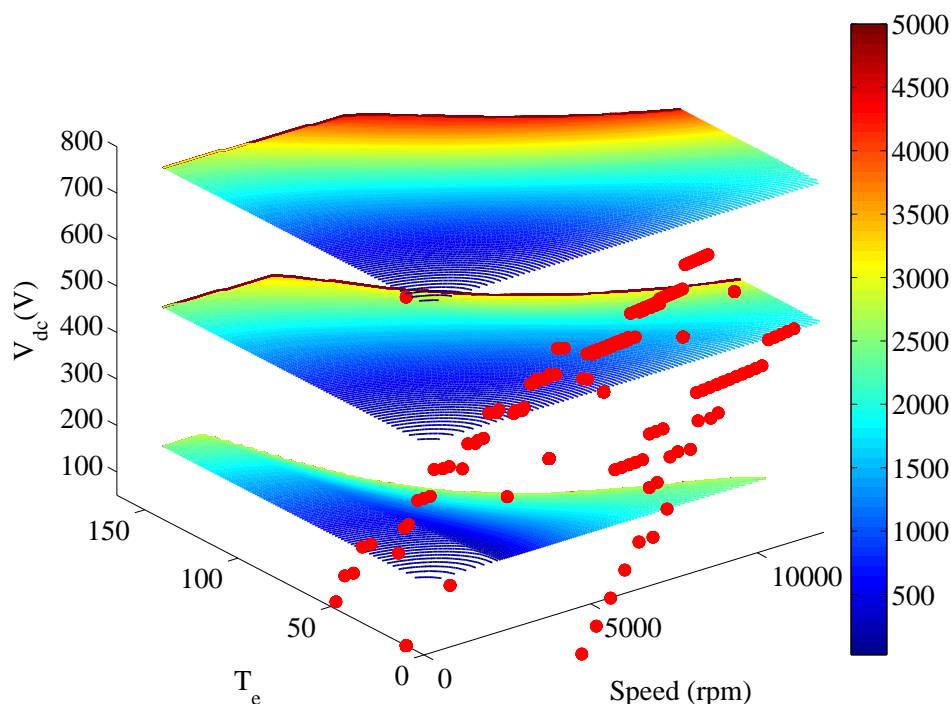


Figure 5.23: Torque - Speed - Dc-link voltage trajectory of running six consequent EUDC drive cycles when using a controllable dc-link voltage, illustrated in different power loss plains

Similar experiment has been done for ECE in an US06 drive cycle and the results are shown for the SiC MOSFET in Table 5.9 and the silicon IGBT in Table 5.10 .

Table 5.9: Drive cycle efficiency of components in various drive cycles with controlled variable dc-link voltage using the SiC based inverter

Drive cycle	Total efficiency(%)	Inverter(%)	Motor(%)	Battery(%)
EUDC(6x)	92.21	98.23	94.53	99.30
ECE(56X)	92.58	98.16	94.59	99.71
US06(6x)	91.38	97.95	93.75	99.51

Table 5.10: Drive cycle efficiency of components in various drive cycles with controlled variable dc-link voltage using the silicon IGBT based inverter

Drive cycle	Total efficiency(%)	Inverter(%)	Motor(%)	Battery(%)
EUDC(6x)	89.26	96.17	94.53	99.30
ECE(56X)	89.54	96.13	94.59	99.72
US06(6x)	88.20	95.75	93.75	99.51

As it can be seen from Table 5.7 to 5.10, having a controllable variable dc-link voltage can improve the total efficiency of the electric drive system. This can be achieved by having a DC/DC converter between the battery and the propulsion inverter. In the SiC MOSFET inverter the drive cycle efficiency is improved between 0.5 to 1 percent whereas in the silicon IGBT based inverter, the efficiency is improved between 1 and 4 percents. This indicates that this controllable variable dc-link method has a bigger impact on the silicon IGBT based inverters. This is mainly due to the fact that a variable dc-link would benefit by decreasing the switching losses. On the other hand a DC/DC converter itself has some losses so the efficiency improvement should be at least as much as the loss introduced by the DC/DC converter. As a result a SiC based inverter with a controllable dc-link system cannot improve the total system efficiency. However for an IGBT based inverter, if the efficiency of the additional DC/DC converter is high enough, this controllable dc-link system can improve the total electric system efficiency.



# Chapter 6

## Conclusions and Future Work

### 6.1 Conclusions

In this Licentiate thesis, the efficiency improvement potential of using SiC materials, different voltage levels, use of overdimensioned components and a variable dc-link in the propulsion inverter is studied. Furthermore an improved current vector control strategy in order to improve the efficiency of the electric drive system is proposed.

The improved current vector control which is obtained from a nonlinear optimization method, increases the motor efficiency in the whole operating region, in particular in the high-speed region, where an efficiency improvement of up to 8% can be achieved. As it can be seen in Table 4.1, for a vehicle equipped with such a motor and current vector control, an average efficiency improvement of about 1.5% is expected in various drive cycles such as NEDC (ECE+EUDC) and US06.

As it was discussed in Chapter 5, by merely replacing the ordinary free-wheeling pn diodes in the propulsion inverter with SiC diodes, the average efficiency is improved about 0.5% in various drive cycles. In another study where SiC MOSFETs are replacing the silicon IGBTs, the average efficiency is increased between 4% to 6% depending on the drive cycle. Furthermore it is shown that by increasing the voltage level of the electric drive system from 400V to 800V may not have a great impact on efficiency for IGBT based inverters. Although the conduction loss may decrease at higher voltages, the switching loss can become more dominant and increase the total loss of the inverter. Overdimensioning the components in the inverter decreases the conduction loss but at the same time it will increase the switching loss. As a result in a SiC MOSFET based inverter with low switching loss, overdimensioning is

shown to improve the average drive cycle between 0.5% to 0.7% percent while in an IGBT based inverter, the improvement is between 0.2% to 0.5%

Finally it is shown that by using a controllable dc-link voltage, the the combined motor and propulsion inverter efficiency can be improved from 0.5% to 1% for a SiC based inverter and 4% to 6% percents for an IGBT based inverter in various drive cycles. Such a controllable dc-link can be achieved by a DC/DC converter between the battery and the propulsion inverter. In the SiC based inverter, the efficiency improvement is not high enough to offset the the losses associated with a new DC/DC converter. So having a controllable dc-link to reduce losses in such inverts is not feasible. However, in the IGBT based inverter with an efficiency improvement of 4%, there is room to add a DC/DC converter without totally offsetting the efficiency improvement.



## 6.2 Future Work

The following items are few examples for continuation of this thesis, either as an complementary solution or in addition to the issues raised in this thesis.

- The PMSM analytical model can be replaced by a FEM model to achieve a more detailed iron loss mapping which will further improve the loss minimization optimization. Furthermore a variable d-q inductance model which is dependent on the current magnitude, would give a more accurate optimization current vector.
- The power electronics components selected for comparisons in this thesis are chosen from already available components in the market. To create in-house developed theoretical designs for comparisons, would be an interesting next step.
- Improving the switching loss modeling by making more measurements and in this obtain a better understanding of switching phenomena, is undoubtedly valuable.
- Since cooling is one the major challenges of electric drives, study of the thermal consequence of different solutions is definitely of great interest. Any solution that improves the efficiency to a level where a cooling system can be simplified or eliminated, can be very valuable from system perspective.
- A complementary Life Cycle Assessment for all efficiency evaluations gives provides a better picture of whether a solution can be commercialized.
- Dc-link capacitors remain a major components in inverters both from weight and cost perspective. A thorough analysis of the dc-link voltage and current is a very beneficial task.
- Investigation of using different frequencies, modulation strategies, variable frequencies.



# Bibliography

- [1] A. Emadi, K. Rajashekara, S. Williamson, and S. Lukic, “Topological overview of hybrid electric and fuel cell vehicular power system architectures and configurations,” *Vehicular Technology, IEEE Transactions on*, vol. 54, no. 3, pp. 763–770, 2005.
- [2] “Tracking progress toward kyoto and 2020 targets in europe,” European Environment Agency, [www.eea.europa.eu/publications/progress-towards-kyoto/download](http://www.eea.europa.eu/publications/progress-towards-kyoto/download), Tech. Rep. 7/2010, 2010.
- [3] Y. Inoue, S. Morimoto, and M. Sanada, “A novel control scheme for maximum power operation of synchronous reluctance motors including maximum torque per flux control,” *Industry Applications, IEEE Transactions on*, vol. 47, no. 1, pp. 115–121, 2011.
- [4] S. Morimoto, Y. Tong, Y. Takeda, and T. Hirasu, “Loss minimization control of permanent magnet synchronous motor drives,” *Industrial Electronics, IEEE Transactions on*, vol. 41, no. 5, pp. 511–517, 1994.
- [5] C. Cavallaro, A. Di Tommaso, R. Miceli, A. Raciti, G. Galluzzo, and M. Trapanese, “Efficiency enhancement of permanent-magnet synchronous motor drives by online loss minimization approaches,” *Industrial Electronics, IEEE Transactions on*, vol. 52, no. 4, pp. 1153–1160, 2005.
- [6] F. Bernal, A. Garefa-Cerrada, and R. Faure, “Loss-minimization control of synchronous machines with constant excitation,” in *Power Electronics Specialists Conference, 1998. PESC 98 Record. 29th Annual IEEE*, vol. 1, 1998, pp. 132–138 vol.1.
- [7] F. Fernandez-Bernal, A. Garcia-Cerrada, and R. Faure, “Model-based loss minimization for dc and ac vector-controlled motors including core saturation,” *Industry Applications, IEEE Transactions on*, vol. 36, no. 3, pp. 755–763, 2000.

- 
- [8] A. Rabiei, T. Thiringer, and J. Lindberg, "Maximizing the energy efficiency of a pmsm for vehicular applications using an iron loss accounting optimization based on nonlinear programming," in *Electrical Machines (ICEM), 2012 XXth International Conference on*, 2012, pp. 1001–1007.
- [9] J. Gallagher and D. Seals, "Design considerations for the power electronics of an electric vehicle propulsion inverter," in *WESCON/94. Idea/Microelectronics. Conference Record*, 1994, pp. 34–40.
- [10] H. Zhang, L. Tolbert, and B. Ozpineci, "Impact of sic devices on hybrid electric and plug-in hybrid electric vehicles," *Industry Applications, IEEE Transactions on*, vol. 47, no. 2, pp. 912–921, 2011.
- [11] B. Ozpineci, L. Tolbert, and S. Islam, "Silicon carbide power device characterization for hev's," in *Power Electronics in Transportation, 2002*, 2002, pp. 93–97.
- [12] B. Ozpineci and L. Tolbert, "Characterization of sic schottky diodes at different temperatures," *Power Electronics Letters, IEEE*, vol. 1, no. 2, pp. 54–57, 2003.
- [13] Y. Cui, M. Chinthavali, F. Xu, and L. Tolbert, "Characterization and modeling of silicon carbide power devices and paralleling operation," in *Industrial Electronics (ISIE), 2012 IEEE International Symposium on*, 2012, pp. 228–233.
- [14] B. Ozpineci, L. Tolbert, S. Islam, and M. Hasanuzzaman, "Effects of silicon carbide (sic) power devices on hev pwm inverter losses," in *Industrial Electronics Society, 2001. IECON '01. The 27th Annual Conference of the IEEE*, vol. 2, 2001, pp. 1061–1066 vol.2.
- [15] H. Zhang, L. Tolbert, B. Ozpineci, and M. Chinthavali, "Power losses and thermal modeling of a 4h-sic vjfet inverter," in *Industry Applications Conference, 2005. Fourtieth IAS Annual Meeting. Conference Record of the 2005*, vol. 4, 2005, pp. 2630–2634 Vol. 4.
- [16] B. Ozpineci, M. Chinthavali, L. Tolbert, A. Kashyap, and H. Mantooh, "A 55 kw three-phase inverter with si igbts and sic schottky diodes," in *Applied Power Electronics Conference and Exposition, 2006. APEC '06. Twenty-First Annual IEEE*, 2006, pp. 7 pp.–.

- 
- [17] H. Zhang and L. Tolbert, "Efficiency of sic jfet-based inverters," in *Industrial Electronics and Applications, 2009. ICIEA 2009. 4th IEEE Conference on*, 2009, pp. 2056–2059.
- [18] O. Hegazy, R. Barrero, J. Van Mierlo, P. Lataire, N. Omar, and T. Coosemans, "An advanced power electronics interface for electric vehicles applications," *Power Electronics, IEEE Transactions on*, vol. 28, no. 12, pp. 5508–5521, 2013.
- [19] K. Acharya, S. Mazumder, and P. Jedraszczak, "Efficient, high-temperature bidirectional dc/dc converter for plug-in-hybrid electric vehicle (phev) using sic devices," in *Applied Power Electronics Conference and Exposition, 2009. APEC 2009. Twenty-Fourth Annual IEEE*, 2009, pp. 642–648.
- [20] O. Hegazy, J. Van Mierlo, and P. Lataire, "Analysis, modeling, and implementation of a multidevice interleaved dc/dc converter for fuel cell hybrid electric vehicles," *Power Electronics, IEEE Transactions on*, vol. 27, no. 11, pp. 4445–4458, 2012.
- [21] M. Pahlevaninezhad, P. Das, J. Drobnik, P. Jain, and A. Bakhshai, "A novel zvzcs full-bridge dc/dc converter used for electric vehicles," *Power Electronics, IEEE Transactions on*, vol. 27, no. 6, pp. 2752–2769, 2012.
- [22] M. Zeraoulia, M. Benbouzid, and D. Diallo, "Electric motor drive selection issues for hev propulsion systems: A comparative study," *Vehicular Technology, IEEE Transactions on*, vol. 55, no. 6, pp. 1756–1764, 2006.
- [23] F. Deng, "An improved iron loss estimation for permanent magnet brushless machines," *Energy Conversion, IEEE Transactions on*, vol. 14, no. 4, pp. 1391–1395, 1999.
- [24] L. Mestha and P. Evans, "Analysis of on-state losses in pwm inverters," *Electric Power Applications, IEE Proceedings B*, vol. 136, no. 4, pp. 189–195, 1989.
- [25] N. Mohan, *Electric Power Systems: A First Course*. Wiley, 2012.
- [26] Z. Zhang, W. Eberle, Z. Yang, Y.-F. Liu, and P. Sen, "Optimal design of resonant gate driver for buck converter based on a new analytical loss model," *Power Electronics, IEEE Transactions on*, vol. 23, no. 2, pp. 653–666, 2008.

- [27] J. Lindström, “An experimental permanent-magnet motor drive – system description and preliminary measurements,” Licentiate Thesis, Chalmers University of Technology, 1999.
- [28] *Technical information FS600R07A2E3*, Infineon, material number:31771, 2012-03-05 Rev 3.0.
- [29] *Datasheet CM300EXS-24S*, Powerex, 2012-07 Rev. 0.
- [30] *Datasheet SCS220AG*, Rohm Semiconductor, 2013-04 Rev. B.
- [31] *Datasheet SCS220KG*, Rohm Semiconductor, 2013-03 Rev. A.
- [32] *Datasheet SCS220KE*, Rohm Semiconductor, 2012-12 Rev. C.
- [33] *Datasheet C4D40120D*, Cree Inc., Rev. -.